BLOOD FLOW DYNAMICS ON A CENTRIFUGALLY ACTUATED MICROFLUIDIC PLATFORM

A thesis submitted towards partial fulfilment of
BS-MS Dual Degree Programme

by

MONIKA DASH

under the guidance of

Professor Suman Chakraborty

Indian Institute of Technology, Kharagpur

Indian Institute of Science Education and Research Pune

Certificate

This is to certify that this thesis entitled "BLOOD FLOW DYNAMICS ON A CENTRIFUGALLY ACTUATED MICROFLUIDIC PLATFORM" submitted towards the partial fulfilment of the BS-MS dual degree programme at the Indian Institute of Science Education and Research Pune represents original research carried out by "MONIKA DASH" at "INDIAN INSTITUTE OF TECHNOLOGY, KHARAGPUR", under the supervision of "Prof. SUMAN CHAKRABORTY" during the academic year 2013-2014.

Student
NAME

Supervisor
NAME

Acknowledgements

I would like to sincerely thank Prof. Suman Chakraborty, my supervisor, for having given me this opportunity to be part of this project which has scope for changing the face of rapid point-of-care diagnostics tomorrow. It has been a nice learning experience fed with his valuable ideas and suggestions.

I am indebted to the Sponsored Industrial Research and Consultancy (SRIC) division, IIT Kharagpur for allowing me to be a part of the IIT community and providing me access to its resources and accommodation facilities. A special thanks to the B.C. Roy Hospital, IIT Kharagpur campus, for timely providing blood samples for the study.

I am grateful to the discussion group on CFD on ResearchGate for their help at various points, especially Mr. Lasse Murtomaki of Aalto University, Finland; who took special interest in this work and helped me a lot with my simulation errors. I am extremely thankful to my friend, Sarfraz Qureshi, IIT Indore; for providing me with a licensed version of COMSOL Multiphysics 4.3a.

During the course of this work, I have interacted and learnt quite a lot from the graduate students here. I would especially like to thank Shantimoy Kar, Nilanjana Bose, Debabrata Dasgupta, Kaustav Chaudhary, Kiran Raj and Adithya Bandyopadhyay for their friendly and valuable help and suggestions. I would also like to thank my friends Saumyadwip Bandyopadhyay, Ishani Chatterjee, Soumya Subudhi, Ashris Choudhury and Tisha Dixit for making my stay enjoyable here.

I thank the Kishore Vaigyanik Protsahan Yojna, Dept. of Science and Technology, Govt. of India; for funding my work and stay. Finally, I would like to express my gratitude to Dr. Arijit Bhattacharyay for kindly co-ordinating my requirements at IISER Pune. I am thankful to IISER Pune for allowing me to work in my field of interest, outside the institute.

Abstract

The viscosity of blood has long been used as an indicator in the understanding and treatment of disease, and the advent of modern viscometers allows its measurement with ever-improving clinical convenience. However, these advances have not been matched by theoretical developments that can yield a quantitative understanding of blood's microrheology and its possible connection to relevant biomolecules[41].
Whole blood (plasma and formed elements together) behaves as a non-Newtonian fluid. The effective viscosity of blood decreases with increasing shear. Relative viscosity of blood is dependent on the concentration of formed elements as well as on the tube diameter in which the flow is being studied. Further, it is also dependent on the endothelial wall characteristics of the tube. This variation of viscosity with shear manifests itself in the bulk flow characters like volumetric flow rate, flow pattern, valve characteristics at capillary joints etc. A major contributor to this behaviour of blood are the red blood cells (RBCs) or erythrocytes, which occupy $\sim$45% of the blood volume. Blood plasma which constitutes the highest fraction of blood $\sim$52% is primarily Newtonian. Upon infection with malaria, the deformability of RBCs change. The deformability is reduced upon infection with *P. falciparum* and enhanced upon infection with *P.vivax*. Our primary focus in this work is *P. falciparum* which is the most popular strain of parasite and also the most lethal. We studied the effect of difference in physical parameters like viscosity arising out of malarial infection or the like to study differences in bulk flow characteristics on a centrifugally actuated microfluidic platform. While there has been substantial amount of work done on dependence of apparent viscosity of blood on hematocrit and tube diameter[45]; there has been no work done , whatsoever, for studying our concerned bulk flow properties in capillary flow based on these dependences. We are concerned with three basic bulk flow properties which are affected by blood rheology and capillary design. These are the burst frequency, volumetric flow rate and capillary filling time. In this work only the first two of these properties are extensively studied. Based on these differences, we propose to build a new inexpensive, rapid point-of-care diagnostic device using a CD based microfluidic platform for diagnosing malaria solely based on rheology dependent flow parameters.
In preparation for the same, microfluidic experiments were conducted using normal blood, malarial blood and blood with hardened RBCs(treated with glutaraldehyde) to measure the frequency of flow burst and volumetric flow rate. Simultaneously, extensive CFD simulations were performed using a finite element method to develop a theoretical or rather, mathematical framework to replicate the experimental observations. Experimental measurements show marked difference in the targeted flow parameters for normal and malaria infected blood/blood with hardened RBCs. The numerical model developed was successfully validated against the experimental observations and existing literature for normal blood at different RBC concentrations. A Newtonian model with higher zero shear viscosity was used to simulate flow of blood with hardened cells which gave a reasonably good match with the experimental data under several assumptions. Extensive experiments need to be performed on malaria infected blood to design an appropriate numerical framework for simulating the same taking into consideration RBC deformability in a continuum Euler-Euler flow model, i.e., without taking particle dynamics of RBCs, effectively reducing the computational expense and expertise requirement. This framework could further be extended to normal blood for better estimation of flow properties.

Contents

Chapter 1

Introduction

This chapter introduces the idea and applications of microscale fluid flows. Different actuation mechanisms are discussed with a special emphasis on Compact Disk based microfluidic systems. The motivation behind the work is stated and advantages of the CD based system are discussed. Based on the context of the existing literature on malarial diagnostics and the different applications of a centrifugally actuated microfluidic system, the aim of the thesis is defined. Finally, outline of the thesis is delineated at the end of this chapter.

1.1 Microfluidics

Microfluidics is the handling and analyzing of fluids in structures of micrometer dimensions. The creation of microfluidic devices began by using technology originally developed for the microchip industry but has now grown into a field of its own [1]. The first applications of microfluidic technologies have been in analysis, for which they offer a number of useful capabilities: the ability to use very small quantities of samples and reagents, and to carry out separations and detections with high resolution and sensitivity, low cost, short times for analysis, and small footprints for the analytical devices [2].
The distant origins of microfluidics lie in microanalytical methods- gas-phase chromatography (GPC), high-pressure liquid chromatography (HPLC) and capillary electrophoresis (CE) - which, in capillary format, revolutionized chemical analysis. These methods (combined with the power of the laser in optical detection) made it possible to simultaneously achieve high sensitivity and high resolution using very small amounts of sample. After the end of the Cold war, it was realized that chemical and biological weapons posed major military and terrorist threats. To counter these threats, the Defense Advanced Research Projects Agency (DARPA) of the US Department of Defense supported a series of programmes in the 1990s aimed at developing field-deployable microfluidic systems designed to serve as detectors for chemical and biological threats. These programmes were the main stimulus for the rapid growth of academic microfluidic technology. The other motivational forces were the advent of molecular biology in the wake of explosion of research interests in genomics in 1980s and the drive for microelectronics with the hope that photolithography and associated technologies that had been so successful in silicon microelectronics and in microelectromechanical systems (MEMS) would be directly applied to microfluidics. Initially started with the use of glass or silicon, the current date microfluidics relies mostly on polymers like polyethylenes in the design of microchannels.

1.1.1 Physics of microfluidics

At the microscale, effects like laminar flow, viscous resistance, diffusion, surface area to volume ratio and surface tension become dominant [3].

Laminar flow

Laminar flow is a condition in which the velocity of a particle in a fluid stream is not a random function of time. Because of the small size, i.e., small width to length ratio of microchannels, flow is almost always laminar [4]. The Reynolds number (Re) for flows in such dimensions, which is given by,

$$Re = \frac{\rho v D_h}{\mu} \tag{1.1}$$

where ρ is the fluid density, v is the characteristic fluid velocity , D_h is the hydraulic diameter and μ is the dynamic viscosity of the fluid; is usually much less than 100, often less than 1.0. For shapes such as squares, rectangular or annular ducts where the height and width are comparable, the characteristic dimension for internal flow situations is taken to be the hydraulic diameter, D_h, defined as:

$$D_h = \frac{4A}{P} \tag{1.2}$$

where A is the cross-sectional area and P is the wetted perimeter. Exploiting the benefits of laminar flow, two or more streams of liquids can flow in the same micro-channel without mixing, except by diffusion, which has been used in micro-devices for performing assays and sorting particles by size. It also allows creation of packets of fluid, which except for diffusive effects, stay relatively well formed and can be moved around in a controlled manner opening up many possibilities in cellular analysis.

Diffusion

Diffusion is the process by which a concentrated group of particles in a volume spread out over time because of Brownian motion so that the average concentration of particles throughout the volume is constant. Diffusion can be modelled in one dimension by the equation,

$$d^2 = 2Dt \tag{1.3}$$

where d is the distance a particle moves in a time t, and D is the diffusion coefficient of the particle. As distance varies to the square power, diffusion becomes very important on the microscale dimensions. As diffusion times in micro-channels can be very short at the microscale, microchannels can be used to generate complex concentration gradients.

Fluidic resistance

The flow rate in a micro-channel is given by,

$$Q = \frac{\Delta P}{R} \tag{1.4}$$

where Q is the flow rate, ΔP is the pressure drop across the channel and R is the channel resistance. For a rectangular microchannel with a low aspect ratio (i.e., w≈h),

the resistance can be found by [4]

$$R = \frac{12\mu L}{wh^3}\left[1 - \frac{h}{w}\left(\frac{192}{\pi^5}\sum_{n=1,3,5}^{\infty}\frac{1}{n^5}tanh\left(\frac{n\pi w}{2h}\right)\right)\right]^{-1} \tag{1.5}$$

and for high aspect ratios (i.e. w $\ll$ h or h $\ll$ w) by

$$R = \frac{12\mu L}{wh^3} \tag{1.6}$$

Similarly effects of greater surface to volume ratios and surface tension help mediate processes like capillary electrophoresis. Surface energies have been exploited in microfluidics by creating virtual walls [5] as well as pumping mechanisms.

1.1.2 Flow actuation mechanisms

Various flow actuation mechanisms have been discussed in the literature in the context of microfluidic transport. These mechanisms have their own potentials and drawbacks. Here, we briefly describe some of the common mechanisms involved in actuating microscale flows.

Pressure driven flow

Pressure driven flows are the easiest and most common means to drive microscale transport. The axial velocity varies quadratically across the channel height, with the maximum velocity at the centerline. This implies a significant dispersion due to considerable variations between wall-adjacent and centerline velocities.

Surface tension driven flow

Surface tension driven flows refer to the actuation and control of fluid transport through a manipulation of the surface tension forces. The manipulation may be hydrodynamic, thermal, chemical, electrical or optical in nature. Since surface tension forces scale with the linear dimensions, these become progressively more dominant with reduction of system length scale from macro to micro and further to nano.

Electrokinetic actuation

Electrical forces may be used to actuate microflows for various lab-on-a-chip based applications, including pumping, mixing, thermal cycling, dispensing and separating. In addition to the fluid mechanical advantages (such as a virtually uniform velocity profile that may be obtained under certain circumstances), electrical actuation and control of microflows exploit several advantageous features of micro- and nano-fabrication technology. In fact, with rapid advancements in miniaturized fabrication technology, integration of micro or nanoscale electrodes in fluidic device has become a simple procedure.

Acoustic streaming

The interaction caused by an external high-frequency oscillation driven by sound or any other obstacles present in the fluid flow leads to this phenomenon.

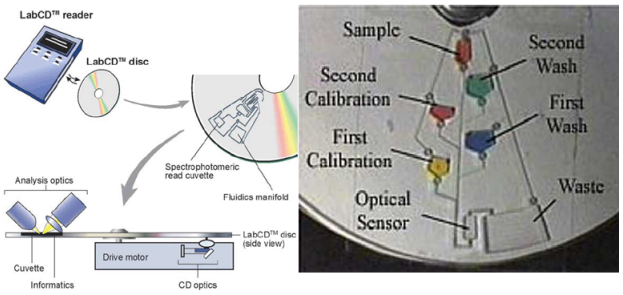

Figure 1.1: A typical design of a Lab-on-a-CD system

All the above methods have their advantages, application specificities and drawbacks in the context of domains of application. Extensive amount of work has been done to assess the same [6-8].

1.1.3 CD based microfluidics

Flows in microchannels can also be rotationally actuated (by the action of centrifugal and coriolis forces) by spinning a disc containing microfluidic networks. Since the platform resembles the compact discs used for data storage, the actuation procedure is called CD based microfluidics. **We have used this mode of actuation in our study**. CD based microfluidics has gained considerable attention owing to its utility in bio-microfluidic analysis. It can act as a relatively inexpensive platform for chemical analysis and biomedical (pathological) diagnostics, exploiting the advantageous features of portability and rapidity of the analytic platform. Its prime advantages lie in handling wide variety of sample types, the ability to gate the flow of liquids, simple rotational motor requirements, economized fabrication methods, large ranges of flow rates attainable, and the possibility of performing simultaneous and identical fluidic operations[9-10].
A number of research investigations have been reported in the literature on several distinctive aspects of rotationally-actuated microchannel flows on CD-based platforms, leading to the common consensus that rotational effects induce an artificial gravity to pump the fluid in the radial direction without pulsation. These advantages render the CD an attractive platform for multiple parallel assays, despite the apparent constraint that the rotational force is essentially a volumetric force that scales with the cube of a characteristic length scale (which may otherwise not sound to be so attractive over the micro-domain, as compared to the surface forces that scale more favourably with linear dimensions). There are two important forces which become important because of the system rotation viz. centrifugal force acting in a radially outward direction and the Coriolis force acting in a transverse direction. Moreover, use of varying rotation speed results in another force due to angular acceleration. In addition, the fluid also experience viscous force which acts to resist its motion. At low rotation speeds, Coriolis force has less contribution over centrifugal force and the flow behaves similar to pressure driven flow. As Coriolis force dominates, a transverse component is introduced into the flow. In multiphase flow, surface tension force also plays a key role in tailoring the fluid flow. All these forces are tuned to achieve desired flow patterns in the microchannels present in a CD-based microdevice. Importantly, forces in the rotating platform are the functions of the rotation speed and the geometry of the channel, which may be altered dynamically with real time monitoring of the system. CD-based microfluidic platforms have two major components :

a polymeric CD and a driving motor. The polymeric CD is fabricated using a lamination technique, which looks very similar to the commercially available data storage disks but contains engraved network of microchannels in it. Different fluidic samples are loaded through the vents into the reservoirs present inside the CD. These are transported to different other reservoirs containing reagents for analysis via the microchannels connecting different reservoirs. Different fluidic operations (like valving, mixing) are also performed in these microchannels. The second major component is the driving motor. The CD is driven by a rotating AC servo motor. The rotor may be programmed at several rotating speeds and tuned to obtain the desired flow characteristics. After the reactions are complete, the readout is taken using a camera to analyse the results of the diagnosis. This uses the forces in rotating platform to drive and manipulate fluid flow.

Advantages of rotationally actuated flow over other actuation methods

- Rotationally-actuated pumping is insensitive to the physicochemical properties of the fluid like ionic concentration or pH, unlike the case with electrokinetically actuated microflows.
- It eliminates the use of tubing, sample loading ports, external valves, splitters and/or syringe connectors, centrifuge tube, glass slides to reduce the cost of different consumables.
- The flow rates induced in a channel by centrifugal forces depend mostly on the channel dimensions and its relative position and orientation to the center of rotation, which varies from 1 nl/sec to 100 μl/sec, a range of volume flow rates cannot be achieved by any other flow actuation mechanism.
- CDs are made from polycarbonate materials which are found to be biocompatible, making it apt for clinical diagnosis. The complete fluidic network can be contained in a single device allowing the provision for multiple parallel assays.
- Operations like valving, volume metering, mixing etc. can be performed easily using centrifugal microfluidics [9,11-14].

1.2 Literature survey on use of CD based microfluidics

Clinical diagnosis of blood involves separation of blood plasma from suspended cells so that they do not interfere in processes like nucleic acid amplification etc. The CD based platform has been successfully implemented in such kind of separation procedures both using small (Haeberle et al., 2006) and large volumes (Amasia and Madou, 2010) of sample.
Mechanical cell lysis for isolating DNA in molecular diagnostic assays has been studied using mammalian (CHO-K1), bacterial (*Escherichia coli*), and yeast (*Saccharomyces cerevisiae*) cells has been demonstrated to be more effective than chemical lysis methods (Jarrell et al., 1992; Gorkin et al., 2010; Kim et al., 2004). To enhance the efficiency of the process, several modifications like use of magnetic blades (Siegrist et al., 2010), lasers (Cho et al., 2007), integration with permanent magnets (Kido et al., 2007) have been incorporated in related works. Thermocycling operation, used for amplification of DNA, has been integrated in a disk based polymerase chain reaction(PCR) for analysis of E.

Coli, with a Peltier thermoelectric device and a thermistor for temperature measurement and control (Kellog et al., 2000).
Enzyme-Linked ImmunoSorbent Assays (ELISA) has been successfully implemented in CD by functionalising the disk surface, spotting directly on it and subsequent reactions to obtain detectable signals from the antigen-antibody complex (Lai et al., 2004). The CD was prepared in PMMA and series of passive valves which released fluids depending on the rotation speed. Fully integrated multiplexed ELISA was demonstrated for rat IgG, running 24 simultaneous assays. Several other immunoassays were reported following this study, which involved targets like Hepatitis A, Tetanus (Riegger et al., 2006), secretory IgA for mental stress (Nagai et al., 2007) and Hepatitis B virus (Lee et al., 2009). Lee et al. (2009) utilized LIFM valve to hold reagents and transfer fluids.
DNA-hybridization in microfluidic system was developed for a compact disc (CD) platform by Jia et al. (2006). Zhao et al. (2006) demonstrated label-free detection using spinning disk interferometery to measure the presence of bound protein, although the sample preparation steps were carried out on a separate platform. Several other such works in biology have been reported in literature using CD based microfluidics over the years.

1.3 Our Motivation and Objective

The *World Malaria Report 2013* issued by WHO [15] shows that even today about 3.4 billion people around the world are at risk of malaria. WHO reports that around 207 million cases of malaria occurred globally in 2012,out of which about 6 million were lethal. Most of these cases ($>$ 80 percent) have been reported in the underdeveloped and developing countries. This happens as a result of lack of fast and inexpensive diagnostic methods. As of today, there are two major diagnostic techniques used for malaria: Blood films and antigen detection tests. While the former is cheap, reliable and provides effective quantitative results about the level of infection, the process involved in between collection of blood sample and deducing conclusive results on malarial infection is an extensive time-taking procedure. On the other hand, the latter is a rapid diagnostic test but is expensive and only provides qualitative results. **We plan to incorporate the benefits of both these methods, i.e., rapid diagnostics with good quantitative results, simultaneously reducing the overall cost of the procedure on a CD based microfluidic platform.** Whole blood (i.e. blood plasma along with suspended formed elements) behaves as a non-Newtonian fluid. The plasma (which occupies $\sim$ 54% of the total volume), by itself, is almost a Newtonian fluid with a very slight viscoelastic character [16]. On the other hand the erythrocytes (RBCs), which occupy 45% of the total blood volume, are deformable, owing to the presence of a spectrin cytoskeleton beneath their lipid bilayer. This deformability of RBCs (diameter ranges between 6-8μm) helps them to pass easily through blood capillaries of diameters $\sim$ 2-3μ. It has been reported in the literature that upon infection with malaria, the deformability of these RBCs change; making them either more deformable or less [17].
We hypothesized to observe a change in effective blood flow characteristics of blood upon infection with malaria as a consequence of change of net blood viscosity owing to the changes in deformabilities of RBCs. Using a CD based microfluidic platform, we intended to compare the difference in three primary non-Newtonian bulk flow parameters of normal and malaria infected human blood:

- Burst frequency/pressure
- Capillary filling time
- Volumetric flow rate

Besides performing experiments using both the types of blood, we also intended to develop a rheological model that could well characterize change in non-Newtonian flow characteristics of blood upon infection with malaria using extensive computational fluid dynamics(CFD) simulations. For doing the same, the unsteady Navier-Stokes(NS) equations are solved with capillary filling effects on a rotating micro-channel, simultaneously taking into consideration the effect of micro-channel dimensions and effective blood hematocrit(volume percentage of RBCs in whole blood). Based on the experimental observations and the numerical model we developed to physically explain our observations on a CD based microfluidic platform, we are motivated to devise a new diagnostic method for detection of malaria that would be fast, provide quantitative results about the level of infection as well as be cheap so that greater section of people around the world can be benefited. The diagnosis will be made solely based on rheology-dependent flow parameters. In the preparation for the design of such a diagnostic device, I performed experiments with several human blood samples (normal and modified with hardened RBCs to consider effects of malarial infection) as well as performed extensive CFD simulations using a finite element method to validate existing rheological models against experimental data within the limits of experimental error and convergence levels. Further, simulations were performed to replicate the measurement of flow burst and the computational model was validated.

Chapter 2 consists of the underlying theory of the involved processes. I discuss the physics behind the primary flow parameters we monitor on a CD based microfluidic platform. Details regarding the several existing non-Newtonian flow models of blood used in the work are also mentioned.

Chapter 3 lists the experimental and numerical methods I have used for the study.

In **Chapter 4**, I put up the primary results of my experiments and numerical simulations, with a detailed physical justification of the same.

I finally summarize my work in **Chapter 5**, also stating the advantages and limitations of the methods used. I also state what further work needs to be done ahead before we can establish the feasibility of development of such a technique for diagnosis of malaria or any other disease that affects blood flow, for that matter.

Chapter 2

Theory

This chapter describes the physical theory underlying the study. The non-Newtonian flow characteristics of fluids are discussed with a special emphasis on blood. Formulation of the different rheological models used to study blood flow is presented and some special features of blood flow are listed. The centrifugal theory is presented showing the effect of the presence of a rotating platform as well as the surface tension effects effecting the flow during transport through the capillary channel are discussed. Finally, the idea of flow burst in passive valves is introduced.

2.1 Non-newtonian fluids

The terminology *non-Newtonian fluids* may apply to a wide range of materials with widely disparate material structure, the main shared characteristic being the inability of the classical linearly viscous Newtonian model to capture the behavior of these fluids. Polymeric liquids, biological fluids, slurries, suspensions, liquid crystals etc. belong to the chass of non-Newtonian fluids [18]. Any fluid must satisfy conservation of momentum.

$$\rho\frac{D\mathbf{u}}{Dt} = -\nabla P + \nabla.\sigma + \mathbf{f} \tag{2.1}$$

where ρ is the density of the fluid, $\mathbf{u}$ is the velocity field, P is the pressure, $\mathbf{f}$ is a body(volume) force and σ is the deviatoric stress tensor (the trace-free component of the stress). Expanding equation 2.1, we get:

$$\rho\frac{\partial\mathbf{u}}{\partial t} + \rho(\mathbf{u}.\nabla\mathbf{u}) = \nabla.[-P\mathbf{I} + \mu(\nabla\mathbf{u} + (\nabla\mathbf{u})^T)] + \mathbf{f} \tag{2.2}$$

Unlike Newtonian fluids, the μ here referring to viscosity of the fluid is not a constant, rather it is a function of certain flow parameters like strain rate; but may or may not be explicitly time dependent. As a result the graph representing the dependence of strain rate on the applied (or pseudo) shear stress(Fig. 2.1) is not linear. This non-linearity gives rise to shear-thinning/thickening characters of non-Newtonian fluids. The main points of deviance of such fluids from non-Newtonian behaviour are: (a) shear thickening/thinning (b) ability to creep (c) ability to relax stresses (d) presence of normal stress differences in simple shear flows (e) presence of yield stress.

Figure 2.1: Shear stress vs. shear strain rate for different kinds of fluids

2.1.1 Rheological models used to study non-Newtonian blood flow

Blood is a viscoelastic, non-Newtonian fluid with specific elements like RBCs, WBCs, platelets and other proteins dispersed in a Newtonian blood plasma. The effective blood viscosity varies with the shear rate. The non-Newtonian characteristics of blood arise out of the presence of various cells in the blood (typically making up 45 percent of the blood volume), which makes blood a suspension of particles. When blood begins to move, these particles (or cells) interact with plasma (which is a Newtonian fluid) and amongst themselves. Hemorheologic parameters of blood include whole blood viscosity which depends on plasma viscosity, red cell aggregation, red cell deformability (or rigidity) and temperature. Listed below are the various models used in this study other than a Newtonian model:

Carreau model

This is the most widely used generalized non-Newtonian fluid model, which defines the viscosity dependent on the strain rate ($\dot{\gamma}$) as follows:

$$\mu_{\text{eff}}(\dot{\gamma}) = \mu_{\text{inf}} + (\mu_0 - \mu_{\text{inf}}) \left(1 + (\lambda\dot{\gamma})^2\right)^{\frac{n-1}{2}} \tag{2.3}$$

where μ_0 is viscosity at zero shear rate(Pa.s); μ_{eff} is viscosity at infinite shear rate(Pa.s); λ is the relaxation time(s) and n is a power index. At low shear rate ($\dot{\gamma} \ll 1/\lambda$), Carreau fluid behaves as a Newtonian fluid and at high shear rate ($\dot{\gamma} \gg 1/\lambda$) as a power-law fluid.

Power-law model

Apparent non-Newtonian viscosity of a power-law fluid is:

$$\mu = m\dot{\gamma}^{n-1} \tag{2.4}$$

where m and n are power law constants. m is a measure of the consistency of the fluid. Higher the value of m , higher is the viscosity of the fluid. n is a measure of the non-Newtonian behaviour of the fluid. Greater the deviation of n from unity, greater is the non-Newtonian behavior.When n<1, the fluid exhibits shear-thinning property and when n>1, it shows shear-thickening property. When n=1, it behaves as a Newtonian fluid. Disadvantages of the power law model are:

1. This model does not have the capability to handle yield stress.

2. It cannot describe the viscosity of various fluids in very low and very high shear rate regions.

Casson model

Introduced by Casson in 1959, this model studies the structure model of the interactive behavior of solid and liquid phases of a two-phase suspension.

$$\mu = \left(\sqrt{\mu_{\text{inf}}} + \sqrt{\frac{\tau_y}{\dot{\gamma}}}\right)^2 \tag{2.5}$$

where, $\mu_{\text{inf}} = \mu_0(1-H)^{-2.5}$ and $\tau_y = 0.01(0.625.H)^3$. It takes care of both yield stress and shear-thinning properties of fluids and hence is a better model.

Generalized power law

The Generalized Power Law model incorporates the Power Law model at low shear rates, the Newtonian model at mid-range and high shear rates and the Casson model as a special case[19].

$$\mu = \lambda|\dot{\gamma}|^{n-1} \tag{2.6}$$

where,

$$\lambda(\dot{\gamma}) = \mu_\infty + \Delta\mu.exp\left[-\left(1+\frac{|\dot{\gamma}|}{a}\right).exp\left(\frac{-b}{|\dot{\gamma}|}\right)\right]; n(\dot{\gamma}) = n_\infty - \Delta n.exp\left[-\left(1+\frac{|\dot{\gamma}|}{c}\right).exp\left(\frac{-d}{|\dot{\gamma}|}\right)\right] \tag{2.7}$$

Walburn-Schneck model

Walburn and Schneck fitted their experimental data obtained from anticoagulated blood with four constants and two parameters (hematocrit H and the sum of fibrinogen and globulin concentrations TPMA) to the following equation:

$$\mu = 0.1C_1.exp(C_2.H).exp(C_4\frac{TPMA}{H^2})\dot{\gamma}^{-C_3H} \tag{2.8}$$

where the four constants are $C_1 = 0.0797$, $C_2 = 0.0608$, $C_3 = 0.00499$ and $C_4 = 14.585$ and TPMA = 25.9 g/L.

2.2 Fahraeus-Lindqvist (FL) effect

"The viscosity of the blood is not a constant quantity, but dependent on the diameter of the tube. Below a critical point at a diameter of about 0.3 mm. the viscosity decreases strongly with reduced diameter of the tube. As a consequence the resistance to the flow of blood in the arterioles (and in the small veins) is considerably less than would be the case if the streaming of the blood followed the law of Poiseuille, i.e., behaved as a fluid with regard to its viscosity [20]". This was the theory established by Fahraeus and Lindqvist to explain flow of blood in narrow tubes in a classic paper in 1931. Fig. 2.2 shows the FL effect as observed under an optical inversion microscope in bright-field during my experiments. The thickness of the cell-free layer goes on increasing with increasing distance from the source reservoir. *Please ignore the length readings on the*

figure, they are of a different calibration scale than the one used here. This observation can be explained on the concept of a plasma-cell free layer, a thin layer adjacent to the capillary wall that is depleted of red blood cells. Because the cell-free layer is red cell-poor, its effective viscosity is lower than that of whole blood. This layer therefore acts to reduce flow resistance within the capillary, with the net effect that the effective viscosity is less than that for whole blood. Because the cell-free layer is very thin (approximately 3 μm) this effect is insignificant in capillaries whose diameter is large. This explanation, while accurate, is ultimately unsatisfying, since it fails to answer the fundamental question of why a plasma cell-free layer exists. There are actually two factors which promote cell-free layer formation.

1. For particles flowing in a tube, there is a net hydrodynamic force that tends to force the particles towards the center of the capillary. This is known as the Segre-Silberberg effect. There are also effects associated with deformability of red blood cells that might increase this force.

2. It is clear that red blood cells cannot pass through the capillary wall, which implies that the centers of red blood cells must lie at least one red blood cell half-thickness away from the wall. This means that, on average, there will be more red blood cells near the center of the capillary than very near the wall.

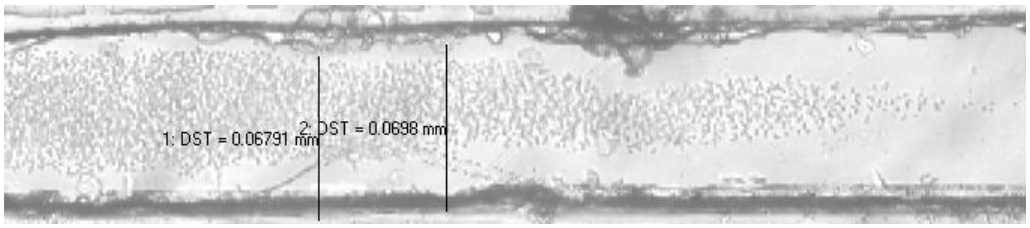

Figure 2.2: FL effect on a microfluidic channel on a CD

Cell-free marginal layer model is a mathematical model which tries to explain Fahraeus-Lindqvist effect mathematically[21]. In small capillary hemodynamics, the cell-free layer is a near-wall layer of plasma absent of red blood cells since they are subject to migration to the capillary center in Poiseuille flow. Cell-free marginal layer model is a mathematical model which tries to explain Fahraeus-Lindqvist effect mathematically.

Governing equations

Considering steady flow of blood through a capillary of radius R, the governing equations for the core region and cell-free plasma region is given by:

$$\frac{-\Delta P}{L} = \frac{1}{r}\frac{d}{dr}(\mu_c r \frac{du_c}{dr}); 0 \leqslant r \leqslant R - \delta \tag{2.9}$$

$$\frac{-\Delta P}{L} = \frac{1}{r}\frac{d}{dr}(\mu_p r \frac{du_p}{dr}); R - \delta \leqslant r \leqslant R \tag{2.10}$$

Using appropriate boundary conditions, the effective viscosity of blood as a function of cell free layer thickness is found to be:

$$\mu_e = \frac{\mu_p}{\left[1 - \left(1 - \frac{\delta}{R}\right)^4 \left(1 - \frac{\mu_p}{\mu_c}\right)\right]} \tag{2.11}$$

FL effect in malarial blood

Considering the increased adhesion of RBCs to the tube walls upon infection with malaria, the wall shear stress experienced by blood in flow increases; simultaneously reducing the thickness of the cell-free layer region. In mathematical terms, δ decreases upon malarial infection; reducing in a greater spread of cells along the width of the channel and hence a reduced FL effect [22].

2.3 Laws of fluid motion: A rotating reference frame

Rotational motion of the fluidic platform induces pseudo forces, which may be experienced by an observer located on a rotating reference frame. Newton's laws of motion in a stationary or fixed reference frame, given by:

$$\overrightarrow{F} = \int_{sys} \overrightarrow{a_{XYZ}} dm \tag{2.12}$$

where a_{XYZ} is the acceleration with respect to the stationary reference XYZ, which has to be related to a_{xyz}, the acceleration with respect to a rotating reference frame xyz (attached to the rotating CD). The origin of xyz is located at a position vector $\overrightarrow{R}$ relative to XYZ. Further, xyz rotates at an angular velocity ω(Fig. 2.3). Thus, the position $\overrightarrow{X}$

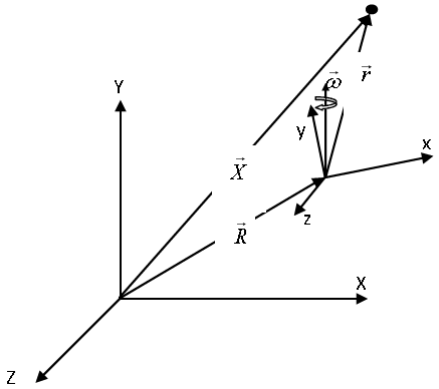

Figure 2.3: The position of a particle from the stationary reference frame (XYZ) and rotating reference frame (xyz)

of a particle relative to XYZ may be related to the position of the same particle having a position of $\overrightarrow{r}$ with respect to xyz as: $\overrightarrow{X} = \overrightarrow{R} + \overrightarrow{r}$. The velocity of the particle in stationary reference frame is denoted by: $\overrightarrow{V_{XYZ}} = \frac{d\overrightarrow{X}}{dt}$ and is related to the velocity in the rotating frame, as

$$\overrightarrow{V}_{XYZ} = \overrightarrow{V}_R + \frac{d\overrightarrow{r}}{dt} \tag{2.13}$$

where, $\overrightarrow{V}_R \left(= \frac{d\overrightarrow{R}}{dt}\right)$ is the velocity of the rotating reference frame with respect to the stationary frame of reference. The term $\frac{d\overrightarrow{r}}{dt}$ may be related to the velocity in rotating frame to obtain:

$$\frac{d\overrightarrow{r}}{dt} = \overrightarrow{V}_{xyz} + \overrightarrow{\omega} \times \overrightarrow{r} \tag{2.14}$$

Substituting eq.(2.14) in eq.(2.13), we obtain an expression relating the velocity in these two frames as:

$$\overrightarrow{V}_{XYZ} = \overrightarrow{V}_R + \overrightarrow{V}_{xyz} + \overrightarrow{\omega} \times \overrightarrow{r} \tag{2.15}$$

For a constant angular velocity, differentiating each term of eq.(2.15), we get:

$$\overrightarrow{a}_{XYZ} = \overrightarrow{a}_R + \overrightarrow{a}_{xyz} + 2\overrightarrow{\omega} \times \overrightarrow{V}_{xyz} + \overrightarrow{\omega} \times (\overrightarrow{\omega} \times \overrightarrow{r}) + \overrightarrow{\dot{\omega}} \times \overrightarrow{r} \tag{2.16}$$

Physically, $\overrightarrow{a}_{XYZ}$ represents the rectilinear acceleration of a particle relative to fixed reference frame XYZ, $\overrightarrow{a}_R$ represents the rectilinear acceleration of the origin of moving frame of reference xyz from the fixed frame XYZ, $\overrightarrow{a}_{xyz}$ represents the rectilinear acceleration of a particle relative to moving reference frame xyz (in rotating frame), $2\overrightarrow{\omega} \times \overrightarrow{V}_{xyz}$ is the Coriolis component of acceleration of the particle experienced in a non-inertial frame of reference, $\overrightarrow{\omega} \times (\overrightarrow{\omega} \times \overrightarrow{r})$ is the centripetal acceleration due to the rotation of the moving frame xyz, and $\overrightarrow{\dot{\omega}} \times \overrightarrow{r}$ is the tangential component of acceleration due to angular acceleration of moving reference frame xyz. From Newton's law, the force acting on a system may be related to the mass of the system(M) and acceleration by eq.(2.12). In the rotating reference frame, the external force F is the sum of net surface forces ($\overrightarrow{F}_s$) and the net body force ($\overrightarrow{F}_b$) acting on a control volume, which may be represented in terms of volume integrations using $dm = \rho d\forall$ as:

$$\overrightarrow{F}_s + \overrightarrow{F}_b - \int_{\forall(sys)} (\overrightarrow{a}_R + 2\overrightarrow{\omega} \times \overrightarrow{V}_{xyz} + \overrightarrow{\omega} \times (\overrightarrow{\omega} \times \overrightarrow{r}) + \overrightarrow{\dot{\omega}} \times \overrightarrow{r}) \rho d\forall = \int_{\forall(sys)} \overrightarrow{a}_{xyz} \rho d\forall \tag{2.17}$$

The right hand side of eq. (2.17) is the rate of change of momentum $\overrightarrow{P}_{xyz}$ of the system measured relative to the frame xyz. Using Reynolds Transport theorem, the above (rate of change of linear momentum with reference to a system, or equivalently, the net force observed from a rotating reference frame) may be expressed in terms of the rate of change of linear momentum relative to a control volume as:

$$\overrightarrow{F}_s + \overrightarrow{F}_b - \int_{CV} (\overrightarrow{a}_R + 2\overrightarrow{\omega} \times \overrightarrow{V}_{xyz} + \overrightarrow{\omega} \times (\overrightarrow{\omega} \times \overrightarrow{r}) + \overrightarrow{\dot{\omega}} \times \overrightarrow{r}) \rho d\forall = \frac{\partial}{\partial t} \int_{CV} \overrightarrow{V}_{xyz} \rho d\forall \tag{2.18}$$

From eq.(2.18), it is evident that the effect of rotating reference frame in momentum conservation may effectively be accounted for in Navier-Stokes eq.(2.2) with three additional terms in body force:

$$\mathbf{f} = -\rho(\overrightarrow{a}_R + 2\overrightarrow{\omega} \times \overrightarrow{V}_{xyz} + \overrightarrow{\omega} \times (\overrightarrow{\omega} \times \overrightarrow{r}) + \overrightarrow{\dot{\omega}} \times \overrightarrow{r}) \tag{2.19}$$

In the present situation, the control volume has no linear acceleration, i.e., $a_R = 0$ and considering the CD rotating in xy plane, the angular velocity may be expressed as: $\overrightarrow{\omega} = \omega\hat{k}$ where $\hat{k}$ is the unit vector in the z-direction. The centrifugal force (when the reference frame is chosen as the rotating frame itself) can be estimated as

$$F_c = \int_{r_{i0}}^{l+r_{il}} (\rho\omega^2 x) h w dx \tag{2.20}$$

where ω is the rotational speed, r_{i0} is the position of the rear end of the meniscus in the inlet reservoir from the centre of rotation and r_{il} is the distance of the inlet of the microchannel from the centre of rotation respectively. Apart from centrifugal force, contributions from Coriolis force and Euler force need to be considered, for high rotation speeds or when the rotation speed varies with time, and may be represented as:

$$F_r = \int_{\forall} -\rho(2\overrightarrow{\omega} \times \overrightarrow{V}_{xyz} + \overrightarrow{\dot{\omega}} \times \overrightarrow{r}) \tag{2.21}$$

2.4 Capillary effects: Surface tension theory and wall adhesion

In order to study the capillary filling dynamics during the motion of blood in the microchannel, I used Level-Set modelling in COMSOL Multiphysics 4.3a. The Laminar Two-Phase Flow, Level Set interface automatically sets up the equations for the convection of the interface. The fluid interface is represented by the 0.5 contour of the level set function ϕ. In air $\phi = 0$ and in blood $\phi = 1$. The level set function can thus be thought of as the volume fraction of blood. The transport of the fluid interface separating the two phases is given by

$$\frac{\partial \phi}{\partial t} + \mathbf{u}.\nabla\phi = \gamma\nabla.\left(\varepsilon\nabla\phi - \phi(1-\phi)\frac{\nabla\phi}{|\nabla\phi|}\right) \tag{2.22}$$

The ε parameter determines the thickness of the interface. When stabilization is used for the level set equation, one can typically use an interface thickness of $\varepsilon = h_c/2$, where h_c is the characteristic mesh size in the region passed by the interface. The γ parameter determines the amount of reinitialization. A suitable value for γ is the maximum velocity magnitude occurring in the model. The density and viscosity are calculated in the following way:

$$\rho = \rho_{air} + (\rho_{blood} - \rho_{air})\phi \tag{2.23}$$

$$\mu = \mu_{air} + (\mu_{blood} - \mu_{air})\phi \tag{2.24}$$

Due to these definitions, the density and viscosity vary smoothly across the fluid interface. The delta function is approximated by

$$\delta = 6|\phi(1-\phi)||\nabla\phi| \tag{2.25}$$

and the interface normal is calculated from

$$\mathbf{n} = \frac{\nabla\phi}{|\nabla\phi|} \tag{2.26}$$

The Navier-Stokes equations (eq. 2.2 along with the mass continuity equation for incompressible fluids $\nabla.\overrightarrow{V} = 0$) describe the transport of mass and momentum for fluids of constant density. In order to account for capillary effects, it is crucial to include surface tension in the model. Gravity effects can be neglected in micro-scale flows (Appendix 2). In the Level Set interface the surface tension force is computed as

$$F_{st} = \nabla.\mathbf{T} \tag{2.27}$$

$$\mathbf{T} = \sigma(\mathbf{I} - (\mathbf{n}\mathbf{n}^T))\delta \tag{2.28}$$

Here, $\mathbf{I}$ is the identity matrix, $\mathbf{n}$ is the interface normal, σ equals the surface tension coefficient (N/m), and δ equals a Dirac delta function that is nonzero only at the fluid interface. When we use the finite element method to solve the Navier-Stokes equations, we basically multiply the equations by test functions and then integrate over the computational domain. If we use integration by parts, we can move derivatives of $\mathbf{T}$ to the test functions. This is used in the Laminar Two-Phase Flow interface and results in an integral over the computational domain plus a boundary integral of the form

$$\int_{\partial\Omega} test(\mathbf{u}).\left[\sigma\left(\mathbf{n}_{wall} - (\mathbf{n}cos\theta)\right)\delta\right]dS \tag{2.29}$$

where θ is the contact angle (see fig. 2.4). If we apply a no-slip boundary condition, the boundary term vanishes because test($\mathbf{u}$) = 0 on that boundary, and we cannot specify the contact angle. Instead, the interface remains fixed on the wall. However, if we allow a small amount of slip, it is possible to specify the contact angle. The Wetted wall boundary condition adds the term given by eq.(2.29) and consequently makes it possible to set the contact angle. The Wetted wall boundary condition is suitable for solid walls

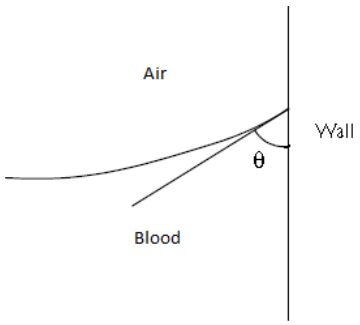

Figure 2.4: Definition of the contact angle θ

in contact with a fluid interface. It sets the velocity component normal to the wall to zero; that is,

$$\mathbf{u}.\mathbf{n}_{wall} = 0 \tag{2.30}$$

and adds a frictional boundary force

$$\mathbf{F}_{fr} = -\frac{\mu}{\beta}\mathbf{u} \tag{2.31}$$

Here, β is the slip length. The boundary condition also allows us to specify the contact angle θ, that is, the angle between the wall and the fluid interface.

2.5 Hydrophobic valving [9]

The pressure drop in a channel with laminar flow is given by the Hagen-Poiseuille equation [23]

$$\Delta P = \frac{12L\mu Q}{wh^3} \tag{2.32}$$

where L is the microchannel length, μ is the dynamic viscosity, Q is the flow rate, and w and h are the channel width and height. The required pressure to overcome a sudden narrowing in a rectangular channel is given by the literature [24]

$$\Delta P = 2\sigma_l cos(\theta_c)\left[\left(\frac{1}{w_1}\right)+\left(\frac{1}{h_1}\right)\right]-\left[\left(\frac{1}{w_2}\right)+\left(\frac{1}{h_2}\right)\right] \tag{2.33}$$

where σ_l is the liquid's surface tension, θ_c is the contact angle, w_1 and h_1 are the width and height of the channel before the restriction, respectively, and w_2 and h_2 are the width and height after the restriction, respectively. In hydrophobic valving, for liquid to move beyond these pressure barriers, the CD must be rotated above a critical speed, at which point the centripetal forces exerted on the liquid column overcome the pressure needed to move past the valve.

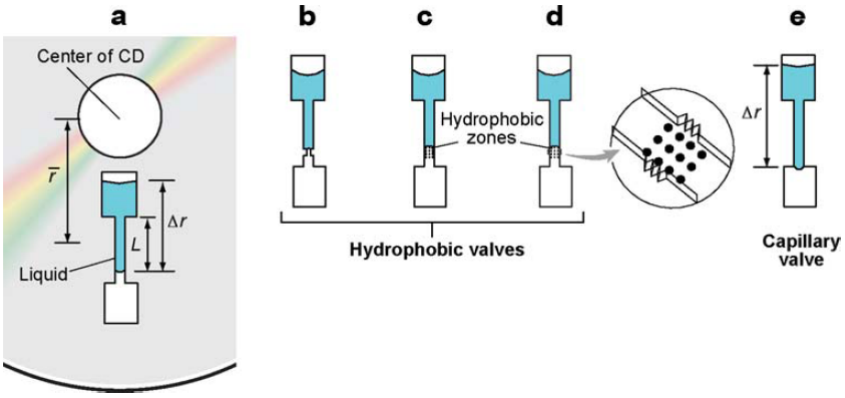

Figure 2.5: (a)Two reservoirs connected by a microfluidic chamber (b),(c),(d) Hydrophobic valves (e) Capillary valve made by a sudden expansion in channel diameter [9]

2.6 Capillary valving [9]

The physical principle involved is based on the surface tension, which develops when the cross section of a hydrophilic capillary expands abruptly, as in fig. 2.5. For capillaries with axisymetric cross sections, the maximum pressure at the capillary barrier expressed in terms of the interfacial free energy is given by [25]

$$P_{cb} = 4\gamma_{al} sin(\theta_c)/D_h \tag{2.34}$$

where γ_{al} is the surface energy per unit area of the liquid-air interface, θ_c is the equilibrium contact angle, and D_h is the hydraulic diameter. Assuming low liquid velocities, the flow dynamics may be modelled by balancing the centripetal force and the capillary barrier pressure (eq. 2.34). The liquid pressure at the meniscus, from the centripetal force acting on the liquid, can be described as follows:

$$P_m = \rho\omega^2\overline{r}\Delta r \tag{2.35}$$

where ρ is the density of the liquid, ω is the angular velocity, $\overline{r}$ is the average distance from the liquid element to the center of the CD, and Δr is the radial length of the liquid sample. Liquid will not pass a capillary valve as long as the pressure at the meniscus (P_m) is less than or equal to the capillary barrier pressure (P_{cb}). Zeng and coworkers[25] named the point at which P_m equals P_{cb} the critical burst condition. The rotational frequency at which it occurs, they called the *burst frequency*. The theoretical burst frequency equation was modified as follows to account for variation of channel cross section:

$$\rho\omega^2\overline{r}\Delta r < 4\gamma_{al} sin(\theta_c)/(D_h)^n \tag{2.36}$$

where n is dependent on the cross-section geometry of the micro-channel.
Duffy et al. [26] modelled capillary valving by balancing the pressure induced by the centripetal force at the exit of the capillary with the pressure inside the liquid droplet being formed at the capillary outlet and the pressure required to wet the chamber beyond the valve. The pressure inside a droplet is given by the Young-Laplace equation [27]:

$$\Delta P = \gamma\left(\frac{1}{R_1} + \frac{1}{R_2}\right) \tag{2.37}$$

where γ is the surface tension of the liquid and R_1 and R_2 are the meniscus radii of curvature in the x and y dimensions of the capillary cross section, respectively. Assuming a small circular cross-section of the capillary and spherical droplet shapes, they derived an expression for critical burst frequency(ω_c) as $a\frac{4\gamma}{D_h} + b$, with the first term on the right representing the pressure inside the liquid droplet being formed at the capillary outlet scaled by a factor a (for nonspherical droplet shapes) and the second term on the right, b, representing the pressure required to wet the chamber beyond the valve. The b term depends on the geometry of the chamber to be filled and the wettability of its walls.

2.7 Finite element method [29]

COMSOL Multiphysics used for numerical simulations in this work, uses the Finite Element method(FEM) for domain discretization and solving partial differential equations (PDEs), in our case the Navier-Stokes equations along with the mass continuity equation in both 2D and 3D microchannels. Its first essential characteristic is that the continuum field, or domain, is subdivided into cells, called elements, which form a grid. The elements (in 2D) have a triangular or a quadrilateral form and can be rectilinear or curved. The grid itself need not be structured.With unstructured grids and curved cells, complex geometries can be handled with ease. This important advantage of the method is not shared by the finite difference method (FDM) which needs a structured grid, which, however, can be curved. The finite volume method (FVM), on the other hand, has the same geometric flexibility as the FEM. The second essential characteristic of the FEM is that the solution of the discrete problem is assumed a priori to have a prescribed form. The solution has to belong to a function space, which is built by varying function values in a given way, for instance linearly or quadratically, between values in nodal points. The nodal points, or nodes, are typical points of the elements such as vertices, mid-side points, mid-element points, etc. Due to this choice, the representation of the solution is strongly linked to the geometric representation of the domain.
The third essential characteristic is that a FEM does not look for the solution of the PDE itself, but looks for a solution of an integral form of the PDE. The most general integral form is obtained from a *weighted residual formulation*. By this formulation the method acquires the ability to naturally incorporate *differential type boundary conditions* and allows easily the construction of higher order accurate methods. The combination of the representation of the solution in a given function space, with the integral formulation treating rigorously the boundary conditions, gives to the method an extremely strong and rigorous mathematical foundation. A final essential characteristic of the FEM is the modular way in which the discretization is obtained. The discrete equations are constructed from contributions on the element level which afterwards are assembled. Reference [29] gives the complete mathematical formulation of the discretization procedure and integration in both the weak and strong forms.

Chapter 3

Methods

This chapter describes the experimental and numerical methods used in this study.

3.1 Experimental methods

3.1.1 Design and Fabrication of CD based microfluidic platforms

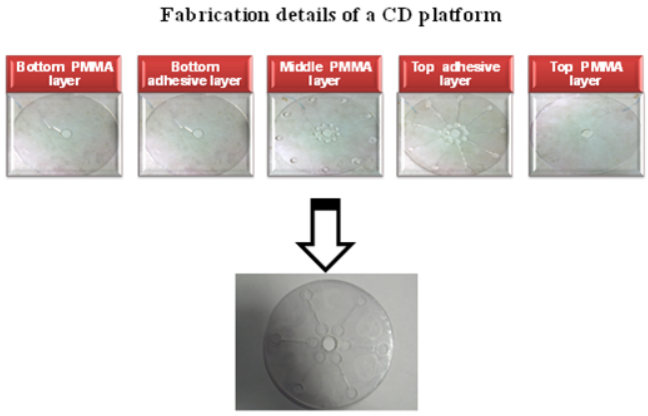

Figure 3.1: Fabrication details of a Lab-on-a-CD device

The figure 3.1 shows the procedure in which a Lab-on-a-CD(LOAC) device is fabricated. As shown in the figure, the platform is prepared by stacking three sheets of Poly(methyl methacrylate) (PMMA) with sheets of pressure sensitive adhesive using a lamination technique. Various diameters of milling bits and drill bits were utilized for the computer numerical control (CNC) micromachining. The design of the channel was made using AutoCAD and fed into the system connected to the CNC. The three PMMA disks constituted the top plate, containing inlet and outlet holes, the middle plate, containing reservoirs, and the bottom plate each of thickness 1 mm, contain the alignment holes at the same position, of the five-layer CD assembly. Each of these plastic plates was bonded by 100 μm thick pressure sensitive adhesive layers (FLEX mount DFM 200 clear V-95, 3M, FLEXcon, Inc., Spencer, MA), in which microchannels were cut through. These channels were aligned with the connecting reservoirs located on the PMMA disks through the alignment holes, and the entire five-layer system was then press-bonded.

The entire CD assembly, after stacking, was subsequently mounted over a programmable ac brushless servo motor (Pacific Scientific, U.S., Model PCM21B, no load speed 13 100 rpm, and peak rated torque 1.3 Nm). The fluid was carefully inserted through the inlet, so that it does not fill the capillary with the aid of surface tension or injection pressure only. The frequency of rotation as well as duration of rotation were fed into the circuit and measurements of linear distance traversed by blood were made after each time interval at varying frequencies of rotation. Images were captured using a bright field on an inverted optical microscope (Olympus IX71) coupled to a monochrome high-speed camera via ProgRes Capture Pro 2.1.
Using the above procedure, micro-channels of 4 different widths were prepared (200, 350, 500, 700 microns).

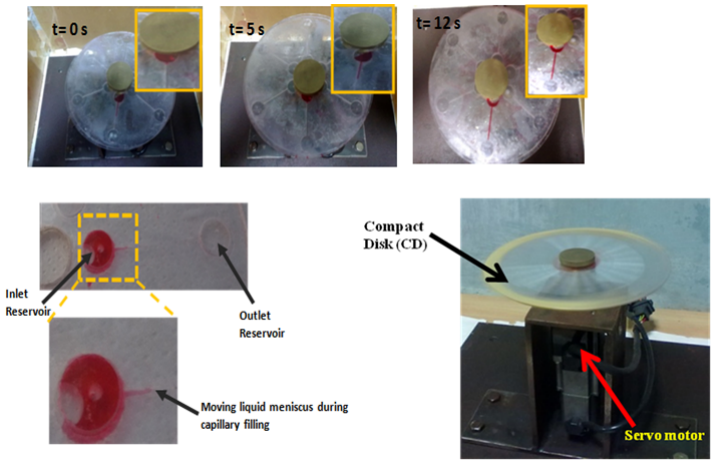

Figure 3.2: Setup for the experiment

3.1.2 Sample preparation

Preparation of PBS buffer

Blood cannot be directly used for the study (which has already been treated with an anticoagulant EDTA), since it is too viscous to flow. Also, the RBCs coagulate together and block flow into the micro-channel. It hence has to be diluted to contain study of flow properties. For the same, a buffer Phosphate-buffered Saline (PBS) is prepared that essentially has the physical and chemical characteristics of human blood plasma. Following is the preparation procedure for the same. For preparing 1 litre of buffer solution with a molar concentration of 0.1M (required concentration), the following are added as per the mentioned weights in distilled water.

1. Disodium hydrogen phosphate (Na_2HPO_4): 1.45 gm
2. Sodium dihydrogen phosphate (NaH_2PO_4): 0.39 gm
3. Sodium chloride (NaCl): 9.02 gm

Preparation of blood samples of varying hematocrit

Blood samples of five different hematocrit values (37%, 41%, 43%, 49%, 51%) were prepared to study the effect of blood hematocrit on net bulk flow properties. Hematocrit

is defined as the volume fraction of RBCs in blood. But here we make an assumption. The blood(which already has been treated with EDTA to prevent coagulation) sample collected from the hospital is directly used for sample preparation; assuming volume of the blood to be effectively equal to the volume of RBCs. In our procedure, it is not possible to directly estimate the percentage of RBCs in the collected blood sample because this blood does not necessarily contain 45% RBCs. But while drawing out blood from the sample using a micro-pipette, care is taken to ensure that the withdrawn volume has a greater concentration of RBCs than plasma. Though, this is not an exact procedure, our primary aim is to compare the effects of different concentrations and that can be done even without extracting out individual RBCs from blood. For preparation of the above mentioned concentrations of samples, required volumes of sample were mixed with requisite volumes of PBS, for e.g., for preparation of a 1 mL sample with 37% hematocrit, 370 μL of blood was taken in an eppendorff and PBS solution was added to it to prepare a net volume of 1 mL. Malarial blood samples were also prepared for testing the same way.

Preparation of samples with hardened RBCs

It has been mentioned in the literature that upon infection with malarial parasite *Plasmodium falciparum*, the stiffness of the RBC cytoskeleton increases resulting in enhanced rigidity and reduced deformability. To test the effects of this on the net blood flow characters, the normal blood samples were treated each with 5 μL of glutaraldehyde (an aldehyde which has long been used as a protein cross linking agent). After the addition of glutaraldehyde, the blood samples are kept at about 4°C for almost a month to harden sufficiently well. The entire sample may get spoilt if the temperature conditions are not maintained sufficiently well over the month.

3.2 Measurement of surface tension coefficent and contact angle of the samples

While the blood passes from the source reservoir into the micro-channel and subsequently into the sink reservoir, there is a three phase contact line at the interface, as shown in fig. 2.4. While blood displaces air to move ahead into the capillary, it wets the solid capillary walls. The blood comes in contact with PMMA on the top and bottom and with PSA in the left and right section of the fluid column. In order to simulate appropriately, the contact angle is measured using a ramé-hart Model 500 goniometer. The associated software DropImage also gives an estimate of the surface tension coefficient when the physical properties like density, viscosity etc. of the concerned materials are fed in. ImageJ was additionally used to calculate the contact angle of equivalent volumes of fluid in contact with both PSA and PMMA using a drop-image analysis via LBADSA fit algorithm that uses the Young-Laplace equation(eq. 2.37) to the image data [28]. The measured values have been tabulated below for the 5 different hematocrit values:

As we observe from the table, the angle of contact with the surface gradually increases with increase in hematocrit value. This directly correlates with the increase in coefficient of surface tension as per the Young-Dupré equation [30,31]. This data is fed as parameters while performing the corresponding CFD simulations.

	Contact angle (in degrees)	Surface tension coefficient (N/m)
PBS on PMMA	59.25 ± 0.01	0.04904 ± 0.00011
H_37 on PMMA	64.95 ± 0.01	0.05079 ± 0.00011
H_41 on PMMA	65.85 ± 0.01	0.05210 ± 0.00011
H_43 on PMMA	66.42 ± 0.01	0.05416 ± 0.00005
H_49 on PMMA	70.79 ± 0.01	0.05538 ± 0.00009
H_53 on PMMA	71.15 ± 0.01	0.06589 ± 0.00218
PBS on PSA	72.25 ± 0.01	0.07608 ± 0.00017
H_37 on PSA	88.74 ± 0.02	0.08204 ± 0.00024
H_41 on PSA	89.23 ± 0.01	0.08278 ± 0.00026
H_43 on PSA	93.82 ± 0.01	0.08331 ± 0.00004
H_49 on PSA	97.74 ± 0.04	0.08593 ± 0.0027
H_53 on PSA	97.74 ± 1.76	0.09531 ± 0.00868

Table 3.1: Contact angle and surface tension coefficient of PBS buffer and samples with varying hematocrit using equal volumes of sample against PMMA and PSA surfaces. Measurement of both were necessary since during the flow, blood comes in contact with both the surfaces. Each measurement was performed 10 times to provide a proper estimate.

3.3 Geometry and meshing for numerical simulation

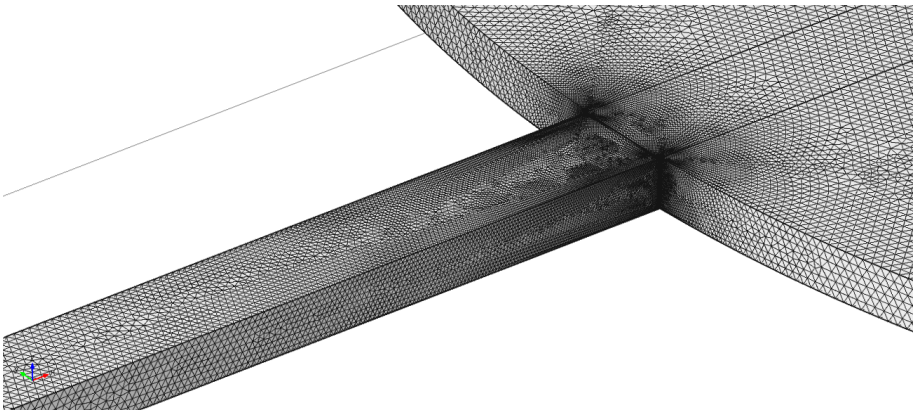

Figure 3.3: A section of a 3D micro-channel design showing an extremely fine finite element meshing at the junction between the micro-channel and fluid reservoir, done using COMSOL Multiphysics 4.3a. The entire design is composed of 13273240 elements (*refer to section 2.7 for definition of an element.*) and the meshing time is 585.67s for a free triangular mesh on my computer with a quadcore i7 processor and 8 GB RAM. This also provides an estimate of the computational expenses on CFD simulations on such 3D meshes. But FEM has an advantage of using unstructured grids over other discretization procedures on curved surfaces as mentioned in the section referenced above. Notice the refinement in element size at the junction which is necessary for an accurate estimate of the flow burst.

2D and 3D geometries of the microfluidic network were created and meshed in COMSOL Multiphysics 4.3a (as shown in Fig. 3.2). The CD is approximately 6 cm in radius. Hence, the microfluidic network is modelled accordingly to be contained inside the CD dimensions. Each fluid chamber is modelled as a cylinder/circle with radius 3 mm for the 3D (height .1 mm which is also the height of the PSA sheet and 2D case respectively. Varying micro-channel widths as mentioned in section 3.1.1 are made. Both the source and sink reservoirs are connected to a venting channel maintained at the atmospheric

pressure to allow air to be removed from the channel and sink as blood moves out of the source into them, displacing air (fig. 3.4). This is required to avoid air locking and bubble entrapment inside the network. It was observed that when the width of the venting channel to the micro-channel connecting the source and sink reservoirs become comparable (precisely when $\frac{d_v}{d_c} < 0.93$, the fluid starts to backflow into the venting channel due to greater capillary effect. This effect was also observed during experiments, since the micro-channels in the CD platforms are prepared by placing two sheets of PSA parallel to each other as per the required width. This leaves an open capillary section connecting the inlet reservoir and the hole which is used to attach the platform to the motor. For the 200 and 350 microns channels, the venting channel was made 500 microns thick and for the other two channels (500 and 700), the width of the venting channel was scaled up accordingly to prevent fluid backflow. The computational domain is set to rotate anticlockwise in order to propel fluid from the source chamber to the sink via the connecting micro-channel.

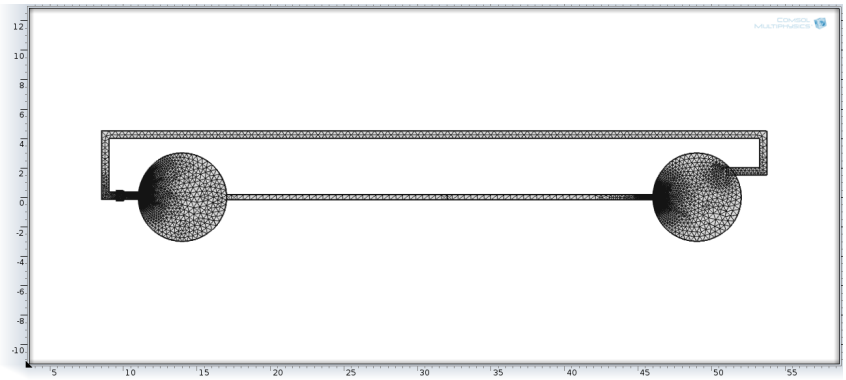

Figure 3.4: A 2D design of the microfluidic network showing the venting channel connected to the source and sink reservoirs. At the start of the simulation, every section of the network is maintained at the atmospheric pressure.

3.4 CFD Simulations

The purpose of CFD simualtion for the microfluidic network(Fig. 3.4) is to calculate the burst frequency of 'passive valves' at the end of each micro-channel. From Table 3.1, it is clear that the valves are not very hydrophilic nor hydrophobic. They are somewhat less hydrophilic. Hence, we are effectively dealing with the case of capillary valves 2.6. Advancement of meniscus under rotation and net capillary filling time are studied. Initially, the source reservoir and half of the capillary are considered to be filled with blood and the rest with air, following the trick used by Kazemzadeh A et. al. (2013) to save computational time[32]. In fact, a few simulations were also performed when only the source reservoir is filled with blood and rest is filled with air but it did not give any significant difference in the measure of flow burst than the case where simulations start when blood is halfway the micro-channel. Rotational speed is increased in steps of 50 rpm starting from 100 rpm to determine the burst frequency. If it still bursts, lower frequencies are considered. Flow is considered laminar as Reynolds number is low in microflows. Reynolds number 1.1.1 of the flow in the micro-channels is much less than 100 and only exceeds it in the reservoirs but stays way below the laminar flow regime

limit, in all the simulations.
Capillary filling dynamics is modelled using the Level-Set method 2.4, while the mass and momentum conservation is governed by the incompressible Navier-Stokes equations (eq. 2.2) and the mass continuity equation. The domain discretization for solving the Navier-Stokes equation to calculate the dependent variables, i.e, velocity and pressure, is done using a P1+P1 discretization mode. P1+P1 means linear elements for both the velocity components and the pressure field. This is the default element order for the Laminar Flow and Turbulent Flow flow interfaces. Linear elements are computationally cheaper than higher-order elements and are also less prone to introducing spurious oscillations, thereby improving the numerical robustness.
The study type is chosen as transient with phase initialization. The Phase Initialization step solves for the distance to the initial interface, D_{wi}. The Time Dependent step then uses the initial condition for the level set function according to the following expression, in domains initially filled with air:

$$\phi_0 = \frac{1}{1 + e^{\frac{D_{wi}}{\varepsilon}}} \tag{3.1}$$

and the following expression in domains filled with blood:

$$\phi_0 = \frac{1}{1 + e^{\frac{-D_{wi}}{\varepsilon}}} \tag{3.2}$$

Time-dependent step is solved using the Generalized-α solver, which is an implicit, second-order accurate method with a parameter called α or p_∞, where $0 \leq p_\infty \leq 1$, to control how much high frequencies are damped. With $p_\infty = 1$, the method has no numerical damping. For linear problems, this corresponds to the midpoint rule. The choice $p_\infty = 0$ gives the maximal numerical damping; for linear problems, the highest frequency is then annihilated in one step. Ref. [33] provides a detailed description of the generalized alpha algorithm used to solve the NS equations. Generalized α by default uses the Constant Newton method as the non-linear solver (*refer to Appendix 1 for a detailed formulation of the same*), which also produces the fastest convergence as compared to non-linear Newton or double dogleg solvers.
Convergence level for inner iterations within each time step is set to 10^{-6} with respect to the relative errors for all the variables. Since interface evolves with time, simulation is run as unsteady using a time step of order 10^{-6}s to maintain low Courant numbers due to stability issues. Capillary force is modelled as implicit body force by specifying wall contact angle and surface tension coefficient between two interacting phases. The centrifugal and Coriolis forces are added as explicit volume forces. To study the effect of Coriolis force on the net flow rate and burst frequency, some simulations were carried out in the absence of the Coriolis force; though it cannot be validated experimentally.
For the validation of the centrifugal theory 2.3, study the effect of centrifugal and coriolis forces on blood flow and also to compare the net bulk flow effects predicted by different rheological models 2.1.1, isolated 3D micro-channels are simulated to solve the Navier-Stokes equations using the following boundary conditions:

1. No slip and no penetration boundary conditions at the walls.

2. The inlet and outlet pressures were set at atmospheric pressure i.e., 103125 Pa.

3. The outlet is set as an open boundary, the flow rates along the grid points on which are integrated to calculate the net bulk flow rate.

4. The inlet is set with a pressure, no viscous stress boundary condition, i.e., $p = p_0$, $\left[\mu\left(\nabla\mathbf{u} + (\nabla\mathbf{u})^T\right)\right].\mathbf{n} = 0$.

While studying the capillary filling dynamics on the actual microfluidic network, the boundary condition on the walls wherever there exists a solid-liquid-air interface is changed to a wetted wall boundary condition with appropriate contact angles. The design and boundary conditions have already been described in detail in the previous section 3.3.
The time dependent solver uses an automatic matrix symmetry condition which detects both symmetric and hermitian matrices. When the discretization of a PDE problem results in a symmetric Jacobian (stiffness) matrix (and a symmetric mass matrix for time-dependent or eigenvalue problems), one can often apply faster and less memory-consuming algorithms to solve the resulting linear systems. But problems in fluid mechanics typically involve non-symmetric Jacobain matrices. COMSOL Multiphysics detects symmetry for both symmetric and Hermitian matrices and takes advantage of the computational savings for a model by utilizing the symmetry. The null-space function is also set to an automatic mode which determines the most appropriate method (orthonormal: uses singular value decomposition or sparse: uses nonlocal couplings) for computation of matrices for constraint handling. The solver automatically handles undefined mathematical functions like division by zero and stops. A direct linear solver is used instead of an iterative one; using an automatic or constant Newton solver to control the damping factor in the damped Newton iterations (Appendix 1). The termination technique is set to Tolerance to terminate the Newton iterations when the estimated relative error is smaller than a specified tolerance. PARDISO is used as the Direct linear solver. PARDISO works on general sparse linear systems of the form Ax = b and uses LU factorization on the matrix A to compute the solution x. In doing so, it uses a preordering algorithm that permutes the columns of A to minimize the number of nonzeros in the L and U factors. A Nested Dissection pre-ordering algorithm is used by the same.
The results obtained from these CFD simulations and simultaneous experiments form the subject matter of the next chapter.

Chapter 4

Results

As described in the methods, blood samples of varying hematocrit were used as samples on a rotating microfluidic platform and the linear distance traversed by them were noted to study the bulk flow rate. The frequency of flow burst was explicitly studied and compared against predictions made using existing theoretical methods. The measurements were made on all four different channels with different widths as mentioned in section 3.1.1. Simultaneously, numerical simulations were performed using the method described in the previous chapter. In this chapter, both experimental and simulation results are presented to validate the numerical model against the experimental data. A few specific experimental observations are stated concerning the RBC dynamics that could have a possible implication on the bulk characteristics. Along with normal blood, corresponding results for the samples with hardened RBCs are discussed. Also, a few observations made using malarial blood are presented.

4.1 Thixotropic characteristic of blood

Non-Newtonian fluids as described in section 2.1 show characteristics of viscous thinning or thickening with increase in shear rate. Blood, being a non-newtonian fluid exhibits a thixotropic or shear-thinning trait. The different models used to describe viscoplastic fluids like blood in section 2.1.1 were used in numerically simulating the flow of blood on a rotating microfluidic platform. The graph below shows how the apparent viscosity of blood varies with shear rate as predicted by these models with reference to a prediction made using a Lattice Boltzmann method by Joshua Boyd et al.(2007)[36].

4.2 Blood flow in a centrifugally actuated rectangular micro-channel

A 3D isolated rectangular micro-channel, as shown in Fig. A.2, was designed using the following dimensions: b = 100 μm and l = 2.9 cm. The widths of the channel was varied (3.1.1) to study the effect of channel width at constant height, also so as to comply with the experiments, neglecting the capillary effects though. As in the actual CD platform, the front of the channel is placed 1.7 cm away from the centre of rotation and is 2.9 cm long. The boundary conditions imposed are as described in section 3.4. All the rheological models listed in section 2.1.1 are used for the study. Also effect of varying hematocrit is studied.

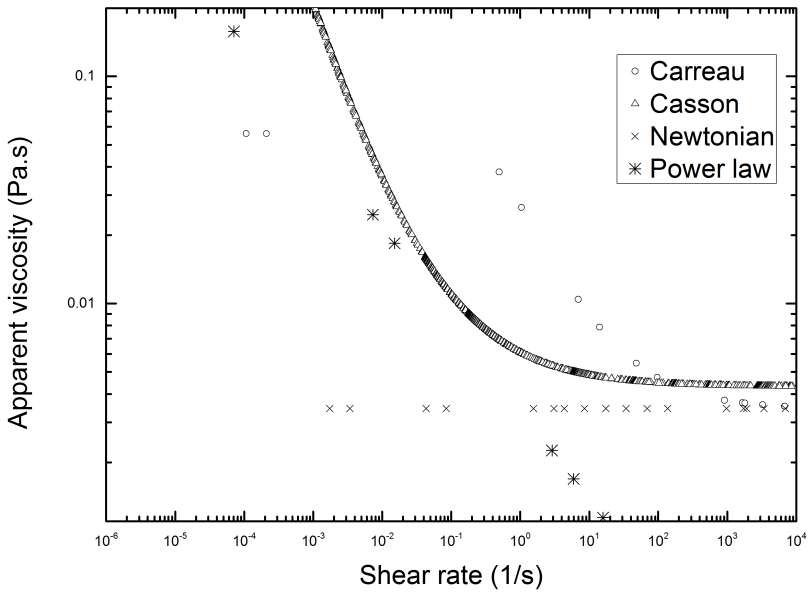

Figure 4.1: Apparent blood viscosity as a function of shear rate. Blood is a thixotropic fluid, as with increasing shear, effective blood viscosity decreases. This is attributed by the Fahraeus-Lindqvist effect and the deformability of suspended elements like RBCs. Different rheological models are used for the estimation as there is no single established model to study blood rheology. The results obtained are in good agreement with those predicted by Boyd et al.[36] and Johnston et al.[38] who used the lattice boltzmann method and finite volume method in human right coronary arteries respectively. While the Carreau and newtonian model tend to converge to a finite and physical value for zero shear viscosity, the power law model fails to do so. The zero-shear viscosity corresponds to the yield stress of blood (i.e. the threshold stress for flow to begin) below which the RBCs aggregate to form stacks of cells called rouleaux.

4.2.1 Pressure variation across the length of the channel

The rotation of the CD creates a gradient in the pressure along the length of the channel, when the pressure at the inlet and the outlet of the channel are same and equal to the atmospheric pressure. This helps the fluid flow inside the channel(Fig. 4.2).

4.2.2 Effect of coriolis force

The velocity-dependent Coriolis force produces an inhomogeneous transverse force in the tangential direction, which has its highest value in the center of the channel. It is also responsible for the flows on rotating channels to be different in terms of pressure distribution, as compared to standard Poiseuille flow. The modification of the velocity profile from a normal parabolic profile is depicted in fig.(4.3a). This effect has been exploited to achieve coriolis mixing of different fluids using rotating microchannels. Being added as an explicit volume force to the model, it also has an effect on the net volumetric flow rate. The different rheological models implicate their effect on the extent of coriolis force differently with the power law, in general, showing more pronounced magnitude of the force as compared to the other models. The magnitude of coriolis force for a given

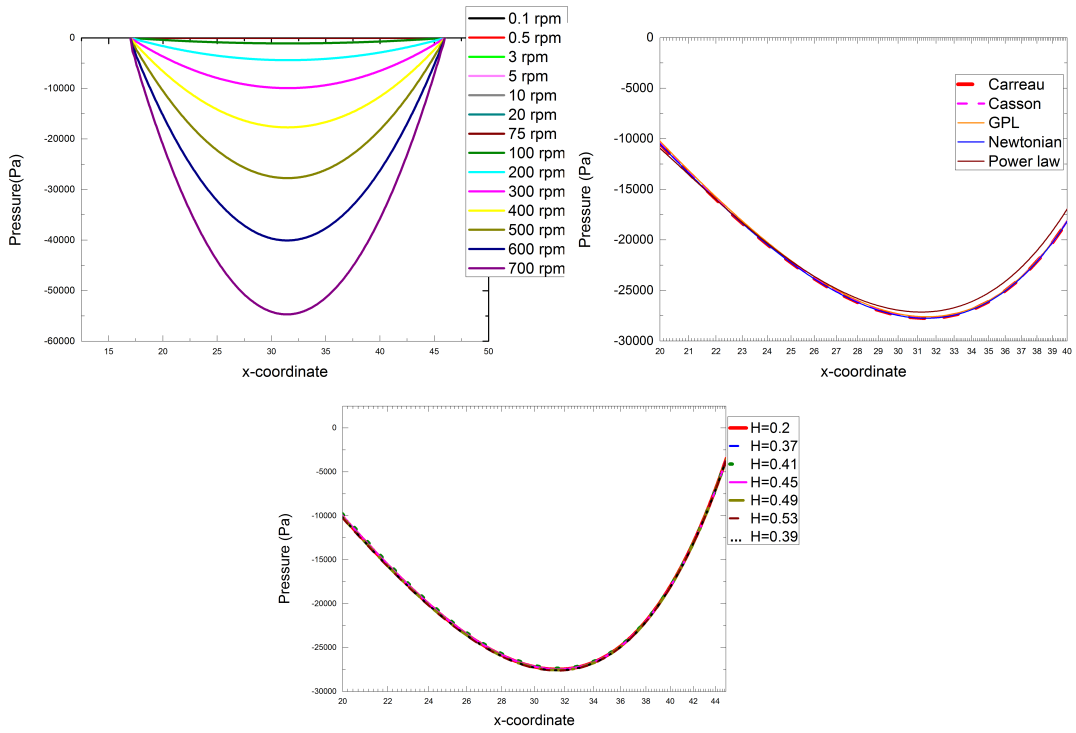

Figure 4.2: (a) Pressure distribution along the length of the channel. A negative pressure gradient in the first half of the channel aids the fluid flow. The results are in good agreement with those presented by Glatzel et. al. [37]. (b) Pressure distribution as predicted using different rheological models for the same channel width (200 μm) and same frequency (500 rpm). Pressure at a point is calculated using a coupled system of mass and momentum conservation equations, which has a direct dependence on viscosity. The difference in pressure as predicted by the different models is very less except for the power law which predicts lower pressure values in the first half and higher values in the second half of the channel. (c) Difference in pressure distribution for different hematocrit for the same frequency, width and rheological model. The difference in the physically relevant range (37% to 55%) is very small.

frequency of rotation also depends on the channel diameter. In fig.(4.3d), the table shows the frequency ranges show when the coriolis force starts to have a visible effect on the flow for the different channel widths.

4.2.3 Effect of varying hematocrit and channel width on volumetric flow rate

Hematocrit, i.e., the volume fraction of RBCs in blood is expected to alter the bulk fluid viscosity. Also, the change of in micro-channel dimensions has an effect on the net volumetric flow rate. Both these effects are studied in this section. The casson model was employed for studying the effect of hematocrit on volumetric flow rate. While COMSOL Multiphysics has models inbuilt to study non-Newtonian flow dynamics via power law model and Carreau model, the formulation for the Casson model is defined into the viscosity value of the fluid using additional parameters like hematocrit and other constants involved in the Casson model.
Assuming uniform thickness, the experimental flow rate is calculated by dividing the volume of fluid that flows into the channel upon rotating the platform for a fixed period

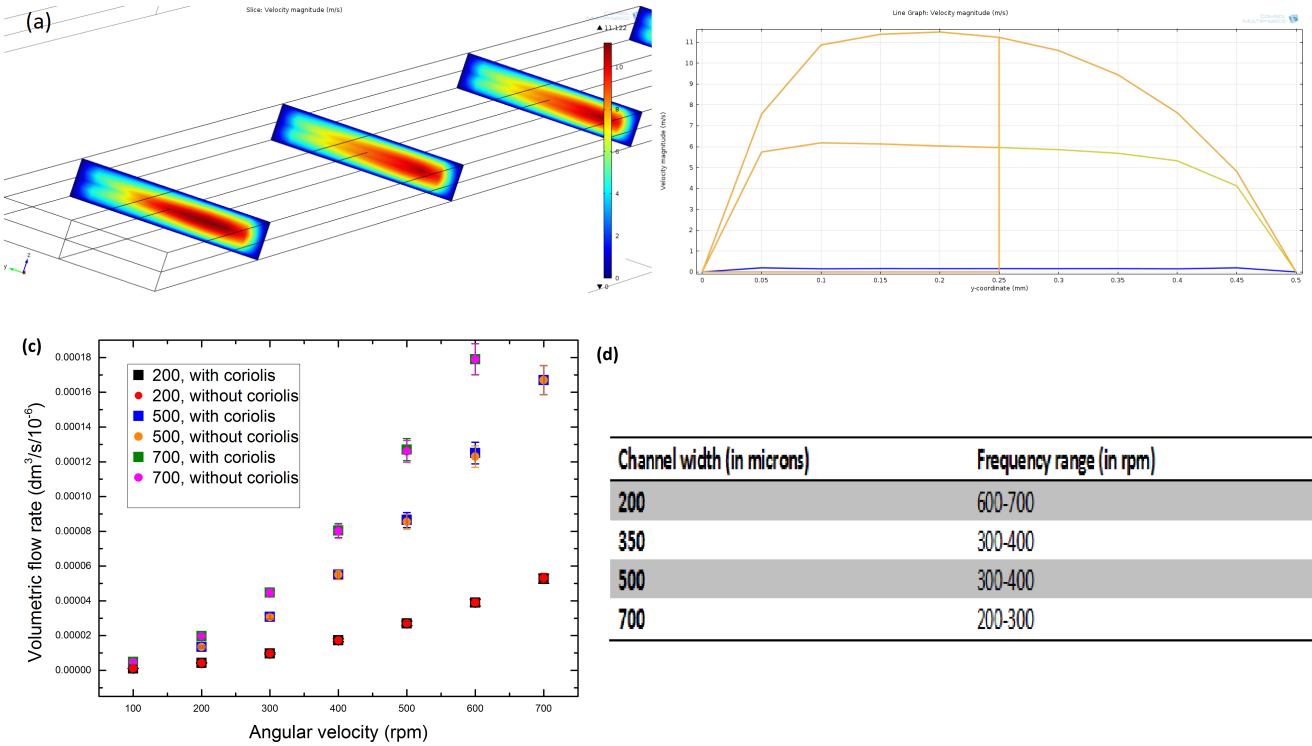

Channel width (in microns)	Frequency range (in rpm)
200	600-700
350	300-400
500	300-400
700	200-300

Figure 4.3: (a) Velocity contour plot showing the effect of coriolis force on the flow pattern. The colour legend on the right indicates the velocity magnitudes corresponding to different colours. Clearly, unlike parabolic flows, the velocity maximum is shifted from the centreline, depending on the direction of rotation. The three slices show the spatial range of maximum velocity narrowing down to a small region, as can be seen in the graph (b) which shows the evolution of velocity profile. (c) The net bulk flow rate is not affected much by the coriolis force in the range of channel dimensions and angular frequencies studied. Numerically, the volumetric flow rate is smaller in the presence of Coriolis force for the 200 microns channel. But surprisingly for the 500 and 700 microns channel, the volumetric flow rate is calculated to be higher in the presence of coriolis force beyond 200 rpm. (d) Effect of coriolis force becomes significant in different frequency ranges for different channel diameters.

of time. Though not an exact procedure, there is no direct way of measurement of flow rate on our current platform. There is no data for frequencies greater than 300 rpm as the fluid has already bursted into the outlet reservoir beyond that and as mentioned, there is no direct way to monitor the bulk flow rate. The volumetric flow rate increases non-linearly with increase in frequency of rotation 4.4. For a given frequency of rotation, increase in feed hematocrit has an inverse effect on the flow rate, i.e. an increase in blood hematocrit reduces the effective blood flow rate. The experimentally measured rates follow the same pattern of rise with frequency as the numerical data. But the magnitudes are relatively small. This is because wall surface tension effects are neglected in the numerical data which effectively act against the flow. Also there is some inherent roughness along the walls of the channel which provide added friction.

As predicted using the Carreau model, the volumetric flow rate increases linearly with an increase in channel width when the height and length are kept fixed 4.5. The other rheological models studied also show a similar variation. Experimental data also verifies the dependence with an almost linear variation. The last data point for flow rate at

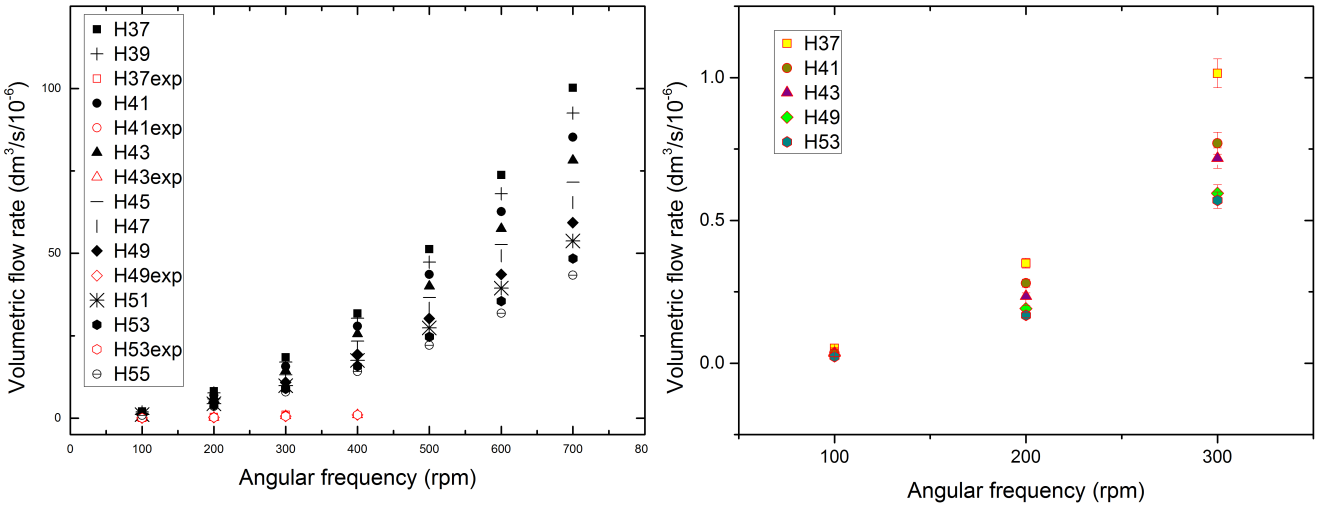

Figure 4.4: (Left) Volumetric flow rate vs. angular frequency for blood samples with varying hematocrit for a channel of 350 microns.(Right) Experimental measure of volumetric flow rate against angular frequency.

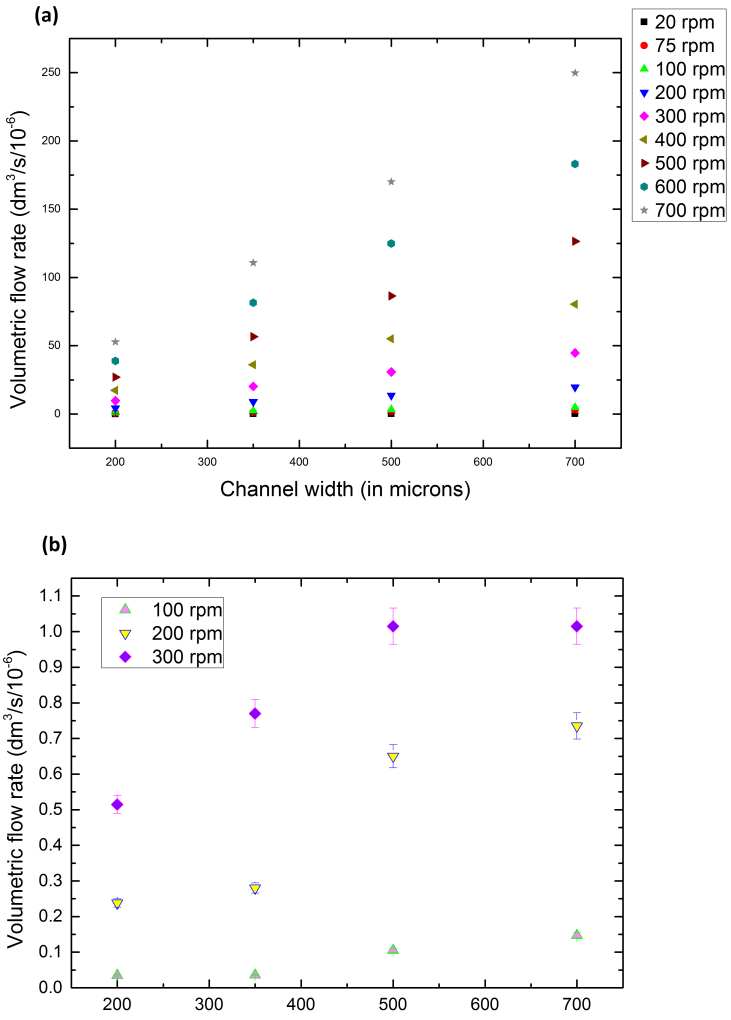

Figure 4.5: Dependence of volumetric flow rate on channel width. (a) Numerical data of flow rate variation with channel width for varying frequencies of rotation. (b) Experimental data

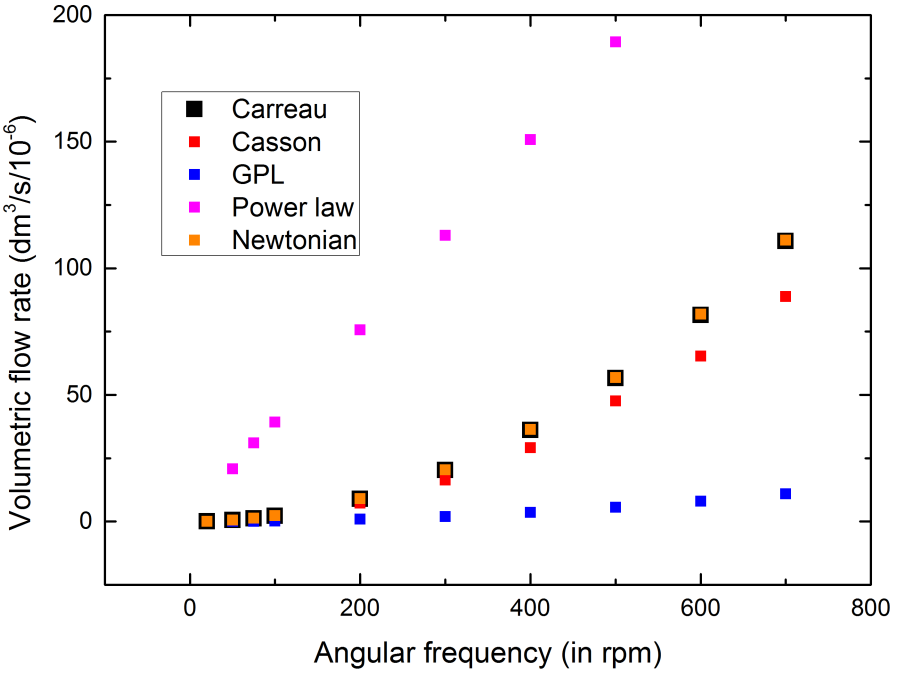

Figure 4.6: Volumetric flow rates as predicted by different rheological models for the same channel dimension 350μm

300 rpm for the 700 microns channel should rather not be included into the dependence estimate as the fluid has already drained into the outlet and there is no direct way to measure the exact flow rate then. The numerical values for the experimental data are smaller than those of the simulation data, probably because of the reasons explained in the previous paragraph.

As shown in Fig. 4.6, different rheological models predict different flow rates for the same channel diameter. The parameters for the study were taken from the data used by Johnston et. al. in their study on right coronary arteries[38]. While the power law over estimates the flow rates, beyond 100 rpm, the Carreau model and the newtonian model essentially predict almost equivalent flow rates. The Generalized power law predicts the least values and provides probably the nearest fit to experimental data but does not have a dependence on the hematocrit. The Casson model has an explicit dependence on blood hematocrit as well as provides the second best fit to experimental data and hence was used for the numerical simulations in predicting the dependence of flow burst on hematocrit.

4.3 Capturing the flow burst: A study of dependence on hematocrit and channel width

Flow in capillary valves is controlled by the interaction between the centrifugal forces and the capillary forces. The fluid advancement in the capillary is stopped when a capillary meets a sudden change in its geometry. The minimum rotational speed required for

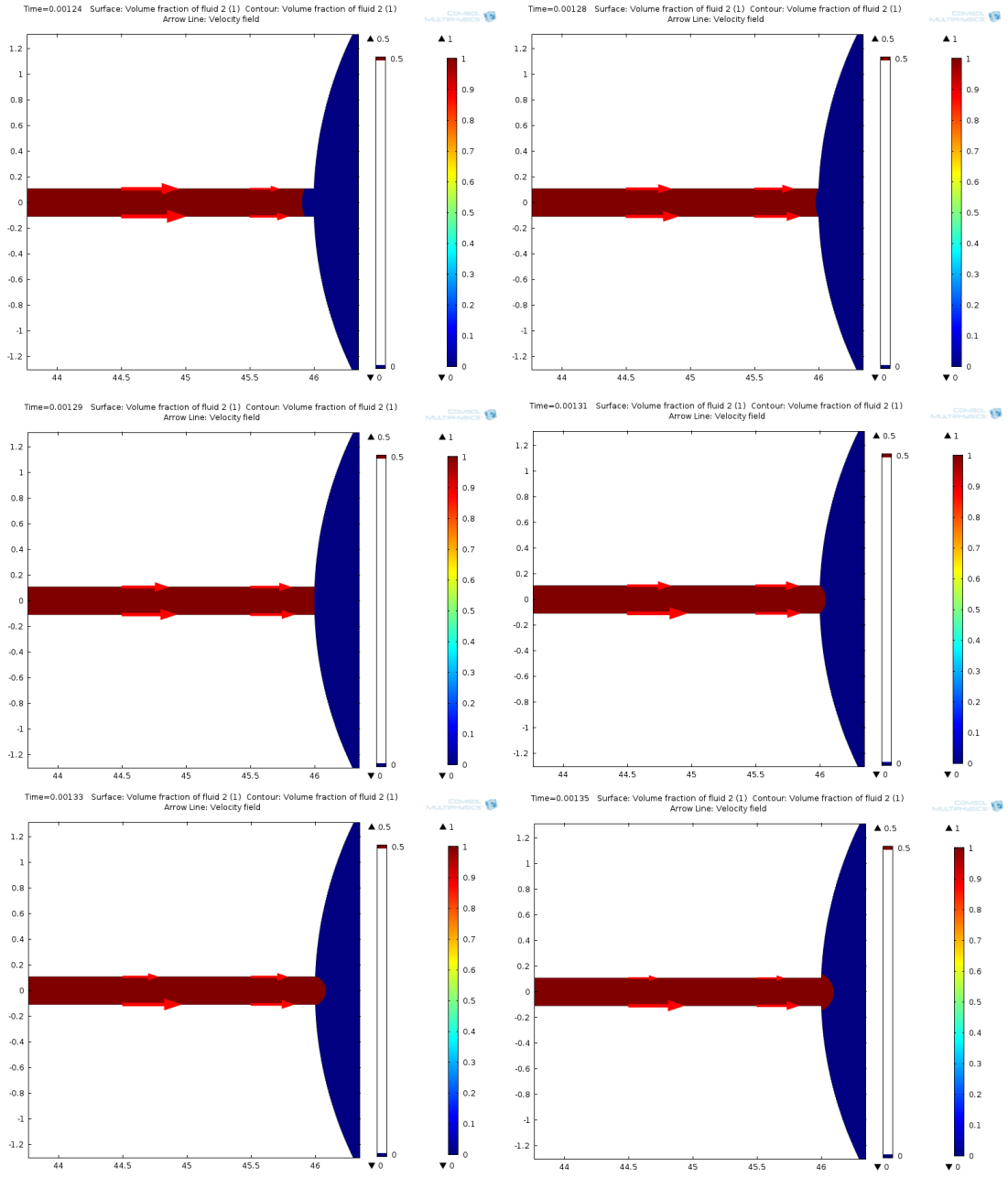

Figure 4.7: Top view of the microfluidic network showing advancement of the fluid meniscus as it faces a sudden change in channel geometry. The red portion shows the volume fraction of blood and the blue portion shows the volume fraction of air that is displaced as blood makes it way from the source to the sink through the micro-channel. The arrows show the velocity field direction. The meniscus changes shape from concave to straight and finally bursts as a convex one into the outlet reservoir while maintaining a static contact angle interface with the walls.

Channel width (in microns)	Experimental Burst (rpm)					Numerical burst (rpm)				
	0.37	0.41	0.43	0.49	0.53	0.37	0.41	0.43	0.49	0.53
200	305	330	333	374	390	300-350	300-350	300-350	350-400	350-400
350	293	306	310	344	362	250-300	300-350	300-350	350-400	350-400
500	279	295	300	339	347	250-300	300-350	300-350	300-350	350-400
700	253	287	294	315	325	200-250	250-300	250-300	300-350	300-350

Table 4.1: Burst frequency of blood samples with varying feed hematocrit as measured for the 4 different channel diameters. In this case, the tube hematocrit has been assumed to be equal to the feed hematocrit.

overcoming that pressure barrier is referred to as the burst frequency. The expression for the modified capillary burst frequency in a 3D non-spherical channel taking into consideration different wall contact angles, is given by [32]:

$$f_b = \left(\frac{\sigma}{\rho \Delta r \overline{r} \left(\frac{2sin\theta}{w} - \frac{2cos\phi_{top}}{h} - \frac{2cos\phi_{bot}}{h} \right)} \right) \tag{4.1}$$

where f_b is the burst frequency, σ is the surface tension coefficient, θ is the contact angle along the side walls and ϕ_{top} and ϕ_{bot} are the contact angles with the top and bottom surfaces. A schematic view of the side and top of the fluid motion in a capillary made of different materials presented in Leu et al. [43] shows that the meniscus is dragged forward at the top and bottom surfaces because of the wetting forces. At the side surfaces, however, the liquid is held back because of its surface tension forces. The burst frequency is calculated by equalizing the centrifugal and the resultant of the surface tension forces. There is no literature where the effect of varying tube hematocrit on burst frequency has been studied. I tried to do the same in the range of hematocrit usually seen in human blood, though in a microfluidic system, it does not need to be the same and can well vary over a wider range. Simulations using the Casson model were performed for the microfluidic network using experimental data and the following results were obtained for the burst frequency for varying hematocrit.

Using equation 4.1 and the data from table 3.1, theoretical predictions for the different hematocrit concentrations were made. Note that blood during its flow in the micro-channel, experiences different boundary conditions in different directions. While, it interacts with PSA on its left and right walls; it moves in contact with PMMA on its top and bottom surfaces. The different contact angles were incorporated into the numerical model using different wetted wall boundary conditions on the walls of the channel and reservoirs. They showed good agreement with the numerical and experimental data with certain deviations, especially when the angle of contact with the PSA sheets becomes a little over 90 degrees,i.e., hydrophobic to some extent. A. Kazemzadeh et al. [32] have

predicted such a discrepancy in the estimates made by the theoretical models in super hydrophilic and less hydrophobic channels. As can be observed from the table, the burst frequency of a given hematocrit concentration decreases with an increase in channel width (for the same height i.e. 100 μm). Similar studies on flow of DI water have been done [32] studying the effect of the aspect ratio (h/w) on the burst frequency. They also reported a similar trend of flow burst for varying widths and a constant height.
The burst frequency, in general, increases with the increase in feed hematocrit. One of the reasons for the same might be the gradual increase in angle of contact of the fluid with the channel walls with the increase in hematocrit. Kazemzadeh et al. [32] predicted a minimum burst frequency for such less hydrophilic micro-channels, beyond which an increase in contact angle results in an increase in the burst frequency. Since, there is no other similar reported literature for blood; we can think based on this idea; that the cases investigated in my experiments have an angle of contact above this minimum contact angle for blood for the range of aspect ratios used.
They also report a leakage in the channel for small contact angles (less than 40^o) arising out of excessive wall adhesion force. Experimentally, I observed similar effects. In cases, where there is improper bonding or when the channel walls are modified by repeatedly passing water through it; the microfluidic network is unable to hold the liquid intact and burst happens even at very low frequencies of rotation $\sim$ 100-150 rpm.
The Casson model used in the numerical simulations for this study, seems to provide a reasonably good measure of the capillary burst as validated against the experimental data. The noticeable change in burst with change in hematocrit and channel widths, though not in a wide range, can be used in the optimal design of channels to map the flow burst onto the effective RBC volume concentration.

4.4 Malarial blood

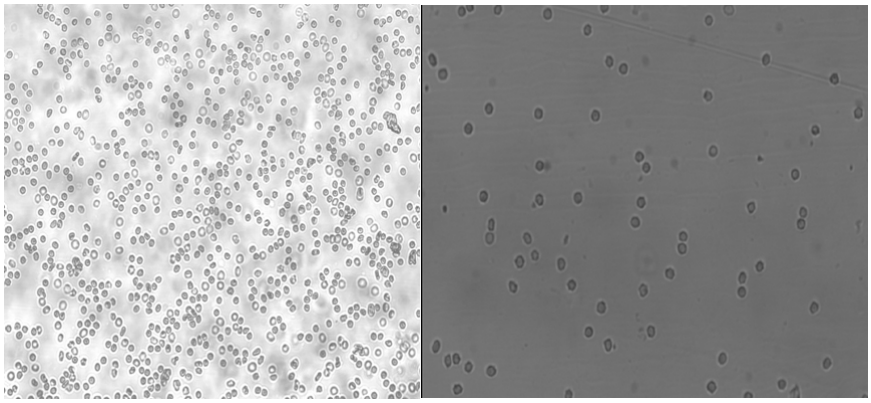

Figure 4.8: (Left) Normal blood (Right) Malaria infected blood. Observed in bright field at 40X under an optical inversion microscope, Olympus IX71

A 40% hematocrit sample of malaria infected blood was prepared using the procedure described in the previous chapter 3.1.2. We received only one malaria positive sample during the project period and hence could not perform extensive tests on malarial blood. This restricted obtaining sufficient data for developing a rheological model involving RBC deformability based on it. The reduced/enhanced deformability of RBCs, enhanced bulk

viscosity and cell-cell interactions upon infection with malaria have been extensively studied and documented in literature, though I did not come across any published data on the dependence of malarial blood viscosity on shear rate a certain parasitemia level [39]. There is substantial amount of data on difference in viscosity of malarial blood at different levels of parasitemia at certain shear rates. The infection also induces enhanced adherence of cells to endothelial walls of tubes. One can clearly observe the difference in the morphological characteristics of normal and malaria infected blood from Fig. 4.8. All these effects would have a manifestation on the bulk flow properties, which we intended to study. In fact, the different RBC motion types like swinging, tumbling, tank-treading seemed restricted in the malarial blood. The flow rates were also recorded to be much lower than normal blood. Repeated tests with the sample that we had at hand, concurrently showed a burst frequency about 100 rpm higher than normal blood. While for the stated hematocrit, in a 700 μm channel, the burst frequency of normal blood was recorded to be in the range of 253-265 rpm; for the malaria infected sample it lied in the range of 384-400 rpm. It is known that the viscosity of blood upon infection with malaria increases by about 1.5 times. The observed difference in burst frequency can be attributed to the enhanced viscosity, though there is no explicit dependence of frequency of burst and viscosity as per the formulation stated in literature [9,41]. Higher viscosity with enhanced cell-wall adhesion would probably require the centrifugal pressure density to be higher than that required by normal blood to overcome the barrier posed by capillary pressure and surface tension. The effect of infection on effective tube fluid density might also be a contributing factor. To confirm these ideas, several tests need to be performed explicitly on malarial blood along with simultaneous numerical simulations to suggest possible development of rheological models. In the absence of malarial blood, I prepared samples of blood with hardened (spectrin cytoskeleton cross-linked) RBCs following the procedure described in 3.1.2. It, more or less, essentially showed Newtonian flow characters as has been detailed in the next section.

4.5 Hardened RBCs

Glutaraldehyde is conventionally used as a cross-linker for hardening RBCs. Hardened RBCs are considered Newtonian [44]. Using numerical data for 10X hardened RBCs from literature [41], and assuming the flow to be Newtonian, numerical simulations were performed which provided an estimate is made against experimental measurements for burst frequency and flow rate. The fig. 4.9 clearly shows the morphological similarity

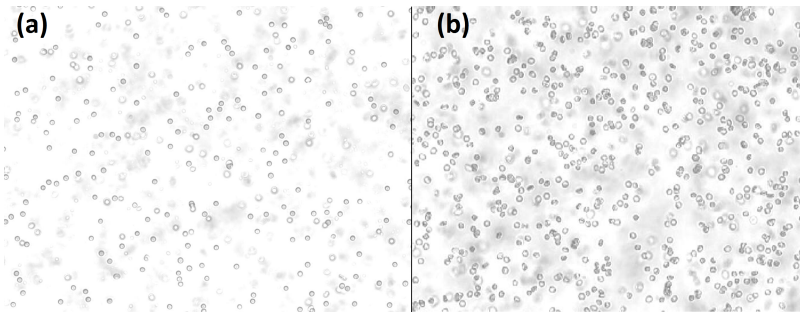

Figure 4.9: (a) Normal blood (b) Blood treated with glutaraldehyde

between the hardened RBCs and malaria infected RBCs, i.e. a wrinkled surface. This

change in morphology along with expected change in stiffness should have an effect on the net bulk flow properties, burst frequency and volumetric flow rate in our case. They were also seen to have restricted motion as compared to normal blood. The dependence of flow rate on angular velocity for varying diameters was seen to be similar as predicted for normal blood. The linear variation of the flow rate on the channel width also stays similar, though the magnitude of the net flow rate is reduced. The primary measurement here concerns the flow burst.

The Newtonian model seems to provide a good enough measure of the flow burst for

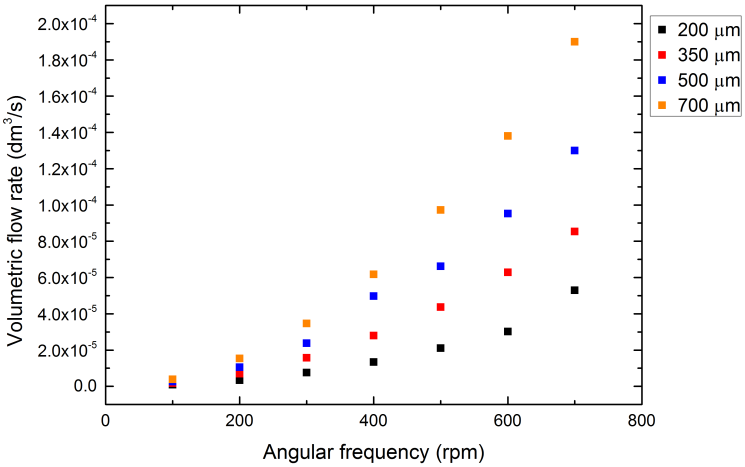

Figure 4.10: Volumetric flow rate as computed using a Newtonian model with viscosity changed as per literature data [41].

Channel width (in microns)	Experimental burst (rpm)					Numerical burst (rpm)
	Hematocrit					
	0.37	0.41	0.43	0.49	0.53	
200	323	336	342	364	378	350-400
350	308	317	322	350	362	300-350
500	298	310	312	345	355	300-350
700	272	295	303	324	332	250-300

Table 4.2: Dependence of burst frequency on blood hematocrit and numerical determination of flow burst using a Newtonian model

the hardened RBCs (Table 4.2). Within the limits of experimental and numerical error, the prediction made by the Newtonian model seems to be a bit off for the low and high ends of hematocrit. This is because the scaled value of viscosity used in the Newtonian model corresponds to a hematocrit of 40% where all the RBCs are assumed to have been hardened uniformly. The effects of increased or decreased RBC concentration or deformability cannot be taken into consideration using a Newtonian model though it is sufficiently reasonable to predict the burst in the most dominant hematocrit range which is around 40%. Malaria does not infect all RBCs at once. Hence, the flow rate and burst, especially for hematocrit in the low and high end of the usual human range, might be considerably different from the values predicted here.

Chapter 5

Summary

5.1 Blood flow on a rotational microfluidic platform

Non-Newtonian blood flow in a centrifugally actuated microfluidic platform was simulated to study effects of coriolis and centrifugal forces. The shear-thinning characteristics of blood was observed from numerical simulations using different rheological models and compared with existing literature. My simulations show a very good match with the numerical estimates of the apparent viscosity predicted using different approaches. The effects of Coriolis force on the flow profile, effective volumetric flow rate and pressure variation along the centreline were studied. It shifts the peak velocity of the flow to one side of the centreline depending on the direction of rotation and does not have much effect on the volumetric flow rate on the range of frequencies studied. The variation of pressure obtained from numerical simulations along the micro-channel centreline was successfully validated against existing literature. The used numerical model to study rotational flow dynamics was hence, justified to be a good one to predict the flow phenomenon.

5.2 Prediction of flow burst against experimental data

The Casson model and the Newtonian model have been successfully demonstrated to provide an adequate estimation of flow burst against the experimental data for blood with normal and hardened RBCs respectively. The burst frequency is seen to decrease with increase in channel width when the channel height and length are kept the same. Burst frequency increases with an increase in blood hematocrit that could be a culmination of effects of change in blood density, viscosity and angle of contact with the side walls. Hardening of cells is seen to increase the frequency of burst for the same hematocrit as normal blood. The parameter considered for this change in the numerical model is viscosity which, assuming a uniform hardening of cells, provides a reasonably good estimate of burst frequency.
Experiments with malarial blood also showed an increase in burst frequency ~ 100 rpm from that of normal blood at the same hematocrit.

5.3 Volumetric flow rate

The different rheological models were used to predict flow rate of blood. Though the Generalized Power Law provided the best estimate against the experimental data, the

Casson model which provided the next best estimate was chosen for maximal use as it has an explicit dependence of blood hematocrit. The volumetric flow rate is seen to increase linearly with channel width with only a varying slope for change in frequency of rotation. Blood with higher hematocrit have been shown to flow at a lower rate than that with a lower hematocrit value both experimentally and numerically. This can be due to the increased viscosity and surface tension forces that act against the centrifugal flow in our case.

5.4 Advantages and disadvantages of the used methods

As stated in the introduction, the CD based microfluidic platform has the inherent advantage of using small sample volumes and providing accurate and rapid quantitative estimates of various flow parameters at the micro-scale. With inexpensive architecture and without any requirement of external driving forces, it provides a reasonable estimate of flow burst and bulk flow rates for comparative studies. The primary disadvanatages at the current state of development of the system is the absence of any method to directly monitor flow velocity or bulk flow rate. The experimental estimates used in this study are based on assumptions of equivalent flow actuation at different channel widths and frequencies and calculated by dividing the distance traversed by the fluid column upon rotation for a fixed time duration. This might not be an appropriate method though it shows good qualitative resemblance with numerical estimates. Therefore, methods need to be developed for simultaneous accurate monitoring of such flow parameters.

5.5 Work ahead

Hardening of cells or infection with malaria has been shown to have an effect on the bulk flow properties of blood, specifically the burst frequency. These characters can hence, be used in medical diagnostics to differentiate normal and infected blood. But to finalize the design and rheological model that could be used as a standard for such diagnostic procedures, many experiments need to be performed with malarial blood with varying RBC concentrations and at different levels of infection. A method needs to be developed for explicit monitoring of the change in viscosity in the flow at varying shear. These viscosity values and corresponding flow rates need to be carefully measured to develop an appropriate mathematical model to describe the rheology of blood using effects of RBC deformability on a continuum scale. The third parameter, capillary filling time, also needs to be documented to study the effect of infection on it.

Bibliography

[1] Fundamentals of Microfabrication. Madou M. 1997. Boca Raton, FL: CRC.
[2] The origins and the future of microfluidics. George M. Whitesides. Nature; Vol 442, July 2006.
[3] Physics and Applications of Microfluidics in Biology. David J.Beebe et al., Annu. Rev. Biomed. Eng. 2002. 4:261 86
[4] White F. 1991. Viscous Fluid Flow. Boston: McGraw-Hill. 2nd ed
[5] Zhao B, Moore J, Beebe D. 2001. Surface directed liquid flow inside microchannels. Science 291:1023 26
[6] Chakraborty, S. (2007), Towards a generalized representation of surface effects on pressure-driven liquid flow in microchannels, App. Phys. Lett., Vol. 90, pp. 034108.
[7] Chakraborty, S, Das, T., Chattoraj, S. (2007), A generalized model for probing frictional characteristics of pressure-driven liquid microflows, J. Appl. Phys., Vol. 102, pp. 10490.
[8] Hunter, R. J. (1989) Foundations of Colloid Science, Oxford University Press, UK.
[9] Madou, M., Zoval, J., Jia, G., Kido, H., Kim, J. and Kim, N. (2006), Lab on a CD, Annual Review of Biomedical Engineering, Vol. 8, pp. 601-628.
[10] Interfacial transport in rotationally actuated microfluidic devices, PhD Thesis, Debapriya Chakraborty (2011), IIT Kharagpur
[11] Ducrée, J., Brenner, T., Haeberle, S., Glatzel, T. and Zengerle, R. (2006), Multil-lamination of flows in planar networks of rotating microchannels, Microfluidics and Nanofluidics, Vol. 2, pp. 78-84.
[12] Haeberle, S. and Zengerle, R. (2007), Microfluidic platforms for lab-on-a-chip applications, Lab Chip, Vol. 7, pp. 1094-1110.
[13] Badr, I. H. A., Johnson, R. D., Madou, M. J. and Bachas, L. G. (2002), Fluorescent Ion-Selective Optode Membranes Incorporated onto a Centrifugal Microfluidics Platform, Anal. Chem., Vol. 74, pp. 5569-5575.
[14] Mark D., Metz, T., Haeberle, S., Lutz, S., Ducrée, J., Zengerle, R. and von Stetten, F. (2009), Centrifugo-pneumatic valve for metering of highly wetting liquids on centrifugal microfluidic platforms, Lab Chip, Vol. 9, pp. 3599-3603.
[15] http://apps.who.int/iris/bitstream/10665/97008/1/9789241564694eng.pdf ; A document publicly released by the World Health Organisation (WHO)
[16] Rheology of Human Blood Plasma: Viscoelastic Versus Newtonian Behavior; M. Brust et al. (2013), Phys. Rev. Lett. 110, 078305.
[17] The Deformability of RBCs parasitized by P.falciparum and P.vivax, Rossarin Suwanarusk et al., The Journal of Infectious Diseases, 2004
[18] Recent Developments in Theoretical Fluid Mechanics: Winter School, Paseky, 1992 by G.P.Galdi, J.Necas
[19] Ballyk PD, Steinman DA, and Ethier CR (1994) Simulation of nonnewtonian blood flow in an end-to-side anastomosis. Biorheology 31(5):565-586
[20] The Viscosity of the blood in narrow capillary tubes; Robin Fahraeus and Torsten Lindqvist, Am J Physiol 96: 562-568, (1931)
[21] Wikipedia: Fahraeus-Lindqvist effect
[22] Quantifying the biophysical characteristics of Plasmodium-falciparum-parasitized red blood cells in microcirculation D. A. Fedosova,b, B. Caswella, S. Sureshc, and G. E. Karniadakisa; PNAS (2011)
[23] Kovacs GTA. 1998. Microfluidic devices. In Micromachined Transducers Sourcebook, Chap. 9, pp. 787-93. Boston:WCB/McGraw-Hill

[24] Madou MJ. 2002. Fundamentals of Microfabrication. Boca Raton, London, New York,Washington DC: CRC Press. 2nd ed.
[25] Zeng J, Banerjee D, Deshpande M, Gilbert JR, Duffy DC, Kellogg GJ. 2000. Design analysis of capillary burst valves in centrifugal microfluidics. Ref. 53, pp. 579-82
[26] Duffy DC, Gills HL, Lin J, Sheppard NF, Kellogg GJ. 1999. Microfabicated centrifugal microfluidic systems: characterization and multiple enzymatic assays. Anal. Chem. 71(20):4669-78
[27] Anderson AW. 1960. Physical Chemistry of Surfaces, pp. 5-6. New York, London, Sidney:Wiley
[28] A Snake-Based Approach to Accurate Determination of Both Contact Points and Contact Angles; A.F.Stalder et al., Colloids And Surfaces A: Physicochemical And Engineering Aspects, vol. 286, no. 1-3, pp. 92-103, September 2006.
[29] Computational Fluid Dynamics: An Introduction; Third edition. by John D. Anderson Jr. et al.
[30] Young, T. Philos. Trans. R. Soc. London 1805,95, 65
[31] Dume. A. Theorie Mechanique de la Chaleur; Gauthier-Villars: Paris, 1869; .pp 36W.
[32] Kazemzadeh A, Ganesan P, Ibrahim F, He S, Madou MJ (2013) The Effect of Contact Angles and Capillary Dimensions on the Burst Frequency of Super Hydrophilic and Hydrophilic Centrifugal Microfluidic Platforms, a CFD Study. PLoS ONE 8(9): e73002. doi:10.1371/journal.pone.0073002
[33] A generalized-α method for integrating the filtered Navier-Stokes equations with a stabilized finite element method; Kenneth E. Jansen et. al., Elsevier.
[34] Jens Ducreé, Stefan Haeberle, Thilo Brenner, Thomas Glatzel, Roland Zengerle, 'Patterning of flow and mixing in rotating radial micro-channels'; Microfluid Nanofluid; 2: 97-105(2006)
[35] Non-newtonian flow simulation in rotating micro-fluidic networks, MTech thesis, Tanveer Ahmed, IIT Kharagpur(2011)
[36] Analysis of the Casson and Carreau-Yasuda non-Newtonian blood models in steady and oscillatory flows using the lattice Boltzmann method; Physics of Fluids (1994-present) 19, 093103 (2007); doi: 10.1063/1.2772250
[37] T.Glatzel and others, "Computational fluid dynamics (CFD) software tools for microfluidic applications - A case study", Computers and Fluids, vol. 37, pp. 218-235, 2008
[38] Non-Newtonian blood flow in human right coronary arteries: steady state simulations; Barbara M. Johnston et al., Journal of Biomechanics 37 (2004) 709-720
[39] Membrane knobs are required for the microcirculatory obstruction induced by Plasmodium falciparum-infected erythrocytes; Carmen Raventos-Suarez et al., Proc. Nadl. Acad. Sci. USA Vol. 82, pp. 3829-3833, June 1985 Medical Sciences
[40] Jens Ducrée, Stefan Haeberle, Sascha Lutz, Sarah Pausch, Felix von Stetten and Roland Zengerle, 'The centrifugal microfluidic Bio-Disk platform'; Micromechanics and Micro-engineering; 17, S103-S115 (2007)
[41] Predicting human blood viscosity in silico; D.A.Fedosov et al., PNAS, 11772-11777, July 19, 2011, vol. 108, no. 29
[42] P. Deuflhard, "A Modified Newton Method for the Solution of Ill-conditioned Systems of Nonlinear Equations with Application to Multiple Shooting," Numer. Math., vol. 22, pp. 289-315, 1974.
[43] Leu TS, Chang PY (2004) Pressure barrier of capillary stop valves in micro sample separators. Sensors and Actuators A: Physical 115: 508-515.
[44] Blood viscosity: Influence of erythrocyte deformation; Shu Chien et al., Science (1967) 827-829
[45] Blood viscosity in tube flow: dependence on diameter and hematocrit; A.R. Pries et.al, American Journal of Physiology (1992)

Appendix A

Appendix

A.1 Appendix 1: Newton's method

The non-linear solver uses an affine invariant form of the damped Newton method [42]. The discrete form of the equations can be written as f(U) = 0, where f(U) is the residual vector and U is the solution vector. Starting with the initial guess U_0, the software forms the linearized model using U_0 as the linearization point. It solves the discretized form of the linearized model $f'(U_0)\delta U = f(U_0)$ for the Newton step δU using the selected linear system solver (f'(U_0) is the Jacobian matrix). It then computes the new iteration $U_1 = U_0 + \lambda\delta U$, where λ ($0 \leq \lambda \leq 1$) is the damping factor. Next, the modified Newton correction estimates the error E for the new iteration U_1 by solving $f'(U_0)E = f(U_1)$. If the relative error corresponding to E is larger than the relative error in the previous iteration, the code reduces the damping factor λ and recomputes U_1. This algorithm repeats the damping-factor reduction until the relative error is less than in the previous iteration or until the damping factor underflows the minimum damping factor. When it has taken a successful step U_1, the algorithm proceeds with the next Newton iteration.

A value of $\lambda = 1$ results in Newton's method, which converges quadratically if the initial guess U_0 is sufficiently close to a solution. In order to enlarge the domain of attraction, the solver chooses the damping factors judiciously. Nevertheless, the success of a nonlinear solver depends heavily on a carefully selected initial guess. Thus one should spend considerable time providing the best value for U_0, giving at least an order of magnitude guess for different solution components.

A.1.1 Convergence Criterion

The nonlinear iterations terminate when the following convergence criterion is satisfied: Let U be the current approximation to the true solution vector, and let E be the estimated error in this vector. The software stops the iterations when the relative tolerance exceeds the relative error computed as the weighted Euclidean norm

$$err = \sqrt{\frac{1}{M}}\sqrt{\sum_{j=1}^{M}\frac{1}{N_j}\sum_{i=1}^{N_j}\left(\frac{|E_{i,j}|}{W_{i,j}}\right)^2} \tag{A.1}$$

Here M is the number of fields; N_j is the number of degrees of freedom in field j. The double subscript denotes degree of freedom index (i) and field (j) component. $W_{i,j} = \max(|U_{i,j}|, S_j)$, where S_j is a scale factor that the solver determines on the basis of a scaling method.

A.2 Appendix 2 : Scaling of forces [35]

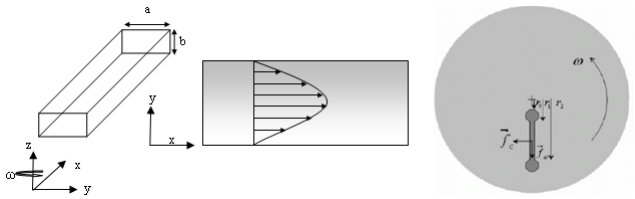

Figure A.1: A rectangular micro-channel cross-section as on a CD platform. A parabolic flow profile of a fluid moving through the channel. The axes have been labelled to illustrate the view orientation.

A rectangular micro-channel of width 'a', height 'b' and length 'l' rotating at an average distance ('$\overline{r}$') from centre of rotation with a speed 'ω', the various force densities in channel are:

1. Average velocity (assuming 2D flow) : $\overline{u} = \frac{\rho\omega^2\overline{r}}{16\mu}a^2$
2. Centrifugal force density due to rotation : $f_\omega = \rho\omega^2\overline{r}$
3. Coriolis force density due to rotation : $f_c = 2\rho\omega\overline{u}$
4. Surface tension density: $f_\theta = \frac{2(a+b)\sigma cos\theta}{abl}$

The ratio of (3)/(2) gives an estimate of the effect of coriolis force/centrifugal force and (4)/(2) gives an estimate of the effect of capillary force/centrifugal force. For graph (A.2), the following parameters were used from literature (interaction of blood with PMMA) to estimate the ratio of forces: $\rho = 1050$ kg/m^3, $\sigma = 0.058$ N/m, $\theta = 3\pi/8$; $l = 2.9$ cm; $b =$ .01 cm; $a =$ .02 cm and $\overline{r} = 1.45$ cm. Gravity effects can be neglected in microfluidic flows because the Bond number in microfluidic flows defined as (force due to gravity/surface tension) $Bo = \frac{\rho g b^2 a l}{2(a+b)\sigma}$ is very low, which using the parameters specified can be calculated as 0.00001715. For the maximum channel width used in my study, i.e. 700 microns, the Bond number is 0.000022509375.

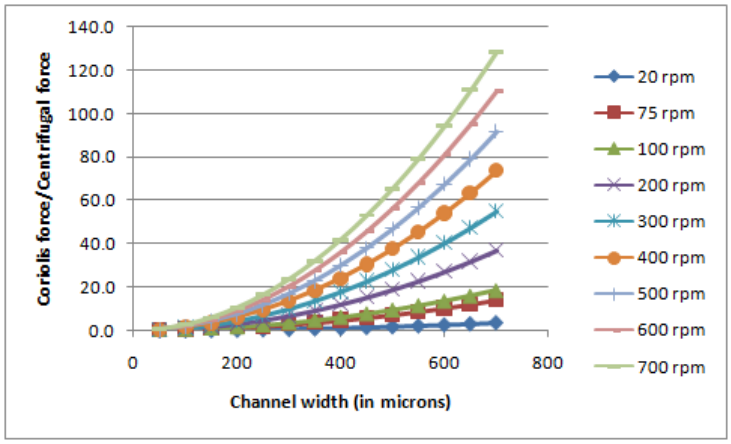

Figure A.2: Ratio of coriolis force effect to that of the centrifugal force effect for a 2D flow. This shows clearly that Coriolis force comes into play only at high frequencies of rotation and higher channel widths. This explains the observations made from the simulation results as presented in Chapter 4.

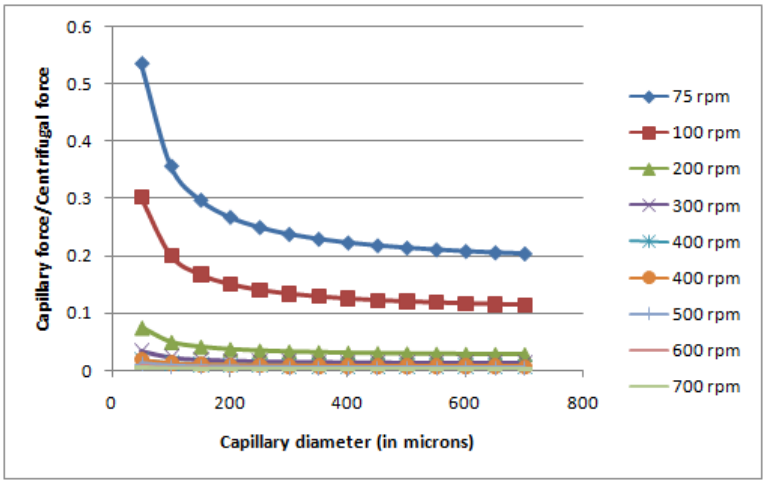

Figure A.3: Ratio of capillary force effects (aided by surface tension) to centrifugal force in a 3D channel. Clearly capillary forces are predominant for smaller channel widths and lower rotation frequencies, otherwise centrifugal force takes over. But even in thinner capillaries, at rotational frequencies higher than 200 rpm, the centrifugal forces are sufficiently strong to neglect the effects of capillary action.